

Rashba spin-orbit interaction in 1-dimensional nanowires

Damaz de Jong

December 16, 2015

Abstract

Now that the first signatures of Majorana zero modes have been observed in experiments, a huge effort towards topological quantum computation is currently underway. Majorana zero modes can appear in nanowire systems, with their topological protection depending on the spin-orbit interaction strength. The spin-orbit interaction strength is therefore a crucial parameter in this experimental field. The largest contribution is expected to be Rashba spin-orbit interaction, which is the subject of this thesis.

Spin orbit interaction in semiconducting systems is governed by symmetry. Spin-orbit interaction is forbidden by symmetry if no additional symmetries are broken in [111] InSb nanowires. Upon reducing the spatial symmetry group, both Dresselhaus and Rashba spin-orbit interaction can emerge in the system. In this thesis a perturbative model for Rashba spin-orbit interaction, which occurs when an electric field reduces spatial symmetry, is developed to predict the interaction strength. This model is then compared to numerical simulations in quantum well systems performed with *Mathematica* and in nanowire simulations performed with *Kwant*.

The model, incorporating the effect of changing geometric dimensions, subband number and the material, shows good agreement with the numerical simulations. Electrical fields resulting from Schrödinger-Poisson simulations are then used to induce Rashba spin-orbit interaction in hexagonal nanowire systems similar to experimental devices again matching the model. Finally, it is shown that the model can be used to calculate results which are intractable to calculate via numerical simulations to find the effect of superconducting coverage of the nanowire on the spin-orbit interaction.

Contents

1	Introduction	4
1.1	Overview of Majorana zero modes	4
1.2	A toy model for Majorana zero modes: The Kitaev chain	5
1.3	Properties of Majorana zero modes	7
1.4	Quantum computation with Majorana zero modes	8
1.5	Experimental realization of Majorana zero modes	10
1.6	Thesis outline	12
2	Symmetry	14
2.1	Representation theory	14
2.2	Application of symmetry to spin	16
2.3	Application of symmetry to exchange statistics	18
2.4	Symmetry and the theory of invariants	19
3	General semiconductor systems	24
3.1	Exposition of spin-orbit interaction	24
3.2	Broken symmetries and spin-orbit interaction	25
3.3	Semiconductor band structures: The Kane Hamiltonian	27
3.4	Application of Löwdin partitioning and theory of invariants	28
3.5	A model for confined systems: Subband Löwdin partitioning	30
3.6	Intermezzo: Bulk inversion asymmetry and Dresselhaus spin-orbit interaction	34
4	Quantum well systems	36
4.1	Theoretical model for quantum well systems	36
4.2	Numerical simulations in reciprocal space	38
4.3	Numerical simulations in real space	40
5	Nanowire systems	45
5.1	Theoretical model for nanowire systems	45
5.2	Method for numerical simulations of 1-dimensional systems	46
5.3	Numerical simulations in constant electric fields	47
5.3.1	Dependence on subband number	48
5.3.2	Dependence on lattice spacing	48
5.3.3	Dependence on growth direction	49
5.3.4	Comparison between nanowire shapes	50
5.3.5	Dependence on Material of the nanowire	52
5.4	Numerical simulations in simulated electric fields	53
5.4.1	Results for $V_{sc} = 0$ V	56
5.4.2	Results for $V_{sc} = 0.2$ V	56
5.4.3	Effects of superconducting coverage	58
6	Conclusion and Outlook	60
6.1	Conclusion	60
6.2	Outlook	61
A	Symbols and Notation	63
B	Units	64

C Exchange statistics of Majorana zero modes	64
D Derivation r_{41}^{6c6c}	66

1 Introduction

1.1 Overview of Majorana zero modes

In 1937, Ettore Majorana published a revolutionary paper proposing a new solution of the Dirac equation. Traditionally, only complex valued solutions to the Dirac equation were investigated, hence predicting an antiparticle for each particle solution. What Majorana realized was that by a suitable transformation the Dirac equation could be made real, which guarantees the existence of a real solution. The particles predicted by this real solution are their own antiparticle and have since been called Majorana fermions [1].

Majorana fermions have been sought as a fundamental particle but have so far not been found, making it unclear if such fundamental particles exist [2]. Alexei Kitaev noticed that Majorana quasiparticles can be fabricated in condensed matter systems as composite particles [3]. The superposition of an electron and a hole indeed leads to a quasiparticle equal to its own antiparticle, which is called *Majorana zero mode* (MZM) or *Majorana bound state*. The term Majorana fermion is also often used, but these quasiparticles are not genuine fermions because normal fermions obey the Pauli exclusion principle while MZMs do not. Moreover, the creation operator of a MZM (which equals the annihilation operator) squares to one instead of zero. The term Majorana fermion does not reflect these properties making the term MZM preferable.

The exchange statistics of MZMs has caused considerable interest in these exotic states. Where the wavefunction of normal fermions only changes sign when two particles are exchanged, MZMs are predicted to obey non-abelian exchange statistics instead. A particle which obeys more general exchange statistics than bosons or fermions is called an *anyon* [4], see also Sec. 2.3. The process of exchanging, or braiding, these particles can lead to elaborate manipulations of the wavefunction which makes MZMs interesting for quantum computing.

Several problems which are intractable to solve on a classical computer could efficiently be solved on a quantum computer. These problems include factoring large integers [5], database searches [6] and simulation of complex physical systems [7]. A quantum computer uses quantum bits, or qubits, instead of normal bits. A qubit is defined as a two level quantum system, but not all such systems are equally useful for quantum computation. For a two level system to be usable as a qubit it must be addressable but stable against environmental noise. The process of information leaking from the qubits to the environment is called *decoherence* and forms a major hurdle towards the realization of a quantum computer. Topological quantum computing uses topology to protect the qubits from decohering. MZMs are expected to exhibit this topological protection because they can only interact with their environment by exchanging their positions or fusing together making them more stable against decoherence [8].

After the theoretical prediction of MZMs, experiments were performed to realize them in the lab. In 2012, the first signatures were seen that would indicate the existence of MZMs [9]. The most definitive proof for their existence would be an experiment in which the exchange statistics are put to the test. Unfortunately, such an experiment has not yet been performed, although huge efforts towards a so called braiding experiment are being made.

For a braiding experiment to work, all elements of that experiment have to work flawlessly. Obtaining a better understanding of the creation process of

the MZMs is therefore an important step in this rapidly developing field. One crucial ingredient for the creation of MZMs in semiconducting nanowires is the so called spin orbit interaction. In this thesis, Rashba spin orbit interaction in nanowires will be investigated after a short introduction into MZMs is given in the remainder of this chapter.

1.2 A toy model for Majorana zero modes: The Kitaev chain

In this section, the toy model devised by Kitaev will be investigated and it will be shown how MZMs appear at the edges of this system. The physical relevance of this toy model will be considered later in Sec. 1.5. The content of this section closely follows reference [10].

MZMs can be realized in a toy model called the Kitaev chain which consists of a 1-dimensional chain of lattice sites. The Hamiltonian of this chain describes an effectively spinless superconducting state. Electrons can move from a site to its neighboring sites with a hopping term t . The energy associated with an electron on a certain lattice site is μ . The superconducting gap is denoted by Δ . In order to write the Hamiltonian in second quantized notation, creation and annihilation operators c_i^\dagger and c_i are introduced. These operators respectively create and annihilate an electron at lattice site i . Denote the number of lattice sites by N . This means that the Hamiltonian can be written as

$$H = -\mu \sum_{i=1}^N n_i - \sum_{i=1}^{N-1} \left(t c_i^\dagger c_{i+1} - \Delta c_i c_{i+1} + \text{h.c.} \right). \quad (1.1)$$

In this equation, h.c. denotes the Hermitian conjugate of the preceding terms. The operator n_i is the number operator on lattice site i . The system under consideration is a spinless system. This means that the Pauli exclusion principle allows only a single electron per lattice site.

Any operator can be split into a real and imaginary part. In particular the electron creation and annihilation operator can be written as:

$$c_i = \frac{1}{2}(\gamma_{2i} + \imath\gamma_{2i+1}), \quad (1.2)$$

$$c_i^\dagger = \frac{1}{2}(\gamma_{2i} - \imath\gamma_{2i+1}), \quad (1.3)$$

where the operators γ_n are real. In other words the N complex operators are expressed by $2N$ real operators. The real operators can be expressed in the complex operators by the inverse transformation:

$$\gamma_{2i} = (c_i + c_i^\dagger), \quad (1.4)$$

$$\gamma_{2i+1} = \imath(c_i^\dagger - c_i). \quad (1.5)$$

It will now be shown that these new operators are in fact Majorana operators by showing that the operators γ_n are hermitian and obey the Clifford algebra, i.e. $\{\gamma_m, \gamma_n\} = 2\delta_{mn}$, where

$$m = 2i + r_1 \text{ with } i \in \mathbb{Z}, r_1 \in \{0, 1\}, \quad (1.6)$$

$$n = 2j + r_2 \text{ with } j \in \mathbb{Z}, r_2 \in \{0, 1\}. \quad (1.7)$$

By definition, γ_n is a real operator, hence it is hermitian, $\gamma_n^\dagger = \gamma_n$. Consider now the anti-commutation relations:

$$\{\gamma_m, \gamma_n\} = (i)^{r_1+r_2} \left[(-1)^{r_1} (c_i c_j^\dagger + c_j^\dagger c_i) + (-1)^{r_2} (c_j c_i^\dagger + c_i^\dagger c_j) \right]. \quad (1.8)$$

By using the normal fermion anti-commutation relations, this can be reduced to:

$$\{\gamma_m, \gamma_n\} = i^{r_1+r_2} [(-1)^{r_1} + (-1)^{r_2}] \delta_{ij} = 2\delta_{mn}. \quad (1.9)$$

This means that the entire system is described in terms of Majorana operators. It is important to note that this can be done with any system of fermions and is not limited to this specific model. The special properties of this system ensure that it is possible to create *localized* Majorana states. To show this, assume that $t = \Delta$ and $\mu = 0$. This means that the Hamiltonian in Eq. (1.1) can be simplified to

$$H = t \sum_{i=1}^{N-1} \left[(c_i^\dagger - c_i)(c_{i+1} + c_{i+1}^\dagger) \right]. \quad (1.10)$$

If the Majorana operators are substituted in this equation the Hamiltonian becomes

$$H = -it \sum_{i=1}^{N-1} [\gamma_{2i+1} \gamma_{2(i+1)}]. \quad (1.11)$$

This Hamiltonian does not depend on the Majorana operators γ_2 and γ_{2N+1} . In other words, the operators γ_2 and γ_{2N+1} commute with the Hamiltonian. These Majorana operators are separated by the entire length of the chain. Each Majorana operator carries half a degree of freedom and is, in a sense, half a fermion. These two Majorana operators can be combined by

$$\tilde{c}_M = \frac{1}{2}(\gamma_{2N+1} + \gamma_0), \quad (1.12)$$

$$\tilde{c}_M^\dagger = \frac{1}{2}(\gamma_{2N+1} - \gamma_0). \quad (1.13)$$

This describes a nonlocal fermion that commutes with the Hamiltonian. This means that if the empty groundstate $|0\rangle$ is considered, a new groundstate $\tilde{c}_M^\dagger |0\rangle$ can be constructed. This state is also at zero energy which means that the groundstate is twofold degenerate. This is called the topological phase of the Kitaev chain.

For the parameters $\mu < 0$ and $t = \Delta = 0$ the system Hamiltonian can be reduced to

$$H = -\mu \frac{1}{2} \sum_i^N (2 + \gamma_{2i} \gamma_{2i+1}). \quad (1.14)$$

Hence all Majorana operators appear in the Hamiltonian and there is no ground-state degeneracy. This state is called the trivial phase.

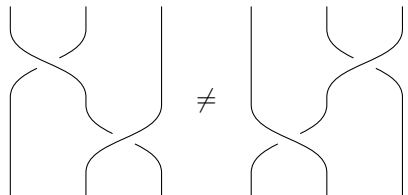
The considerations presented above are not only valid for the special values of μ, t and Δ used here. For parameter values that are close enough, the delocalized MZMs also appear at the edge of the chain when $|\mu| < 2t$.

1.3 Properties of Majorana zero modes

In the previous section it was found that two Majorana zero modes could appear at the edge of a 1-dimensional chain. In this section more properties of the Majorana zero modes will be discussed.

The exchange statistics of MZMs is an important motivation for investigating them. Fundamental particles are either bosons or fermions (see Sec. 2.3). Exchanging a pair of bosons leaves the wavefunction unchanged while exchanging a pair of fermions multiplies the wavefunction by -1 . The reason that a wavefunction normally cannot be changed by an arbitrary phase is that exchanging a pair of particles twice must be equal to doing nothing. There are however some exceptions; exchanging a pair of particles twice around a vortex does not necessarily yield the identity. These so called anyons can emerge in condensed matter systems. Abelian anyons are particles that change the wavefunction by a phase θ upon exchanging two of these particles.

Non-abelian anyons can also emerge in these systems. In this case the operations exchanging pairs of particles do not commute between themselves. A good way to visualize the exchange of particles is to draw the world line of these particles. Hence particles are represented as strings going from top to bottom representing the flow of time. Exchanging particles then leads to braiding of the world lines.


(1.15)

The non-abelian nature of the exchange process is shown in Eq. (1.15). The braiding of n particles is described with the braid group \mathcal{B}_n . As will be shown in Sec. 2.3, representation theory can describe the result of braiding when the number of particles is fixed.

For MZMs, the result of exchanging them can be calculated. It turns out that the Majorana operators of the previous section obey non-abelian braiding statistics [11]. This means that the permutation group can no longer be used to faithfully describe an exchange of particles. Instead the more general braid group \mathcal{B}_n has to be used. The proof that MZMs obey non-abelian exchange statistics can be found in appendix C. The unitary operator representing the exchange of MZMs γ_i and γ_j is [12]:

$$U = e^{i\phi} e^{\pi\lambda\gamma_i\gamma_j/4}, \quad (1.16)$$

where λ is an arbitrary sign depending on the direction of rotation. The factor ϕ denotes an extra abelian phase and is often omitted from the braiding result, as an overall phase is not observable.

By combining Majorana zero modes in a way similar to Eq. (1.12) a number operator can be constructed by $\tilde{c}_M^\dagger \tilde{c}_M$. This operator has the eigenvalues 0 and 1, suggesting the interpretation that 2 MZMs can together either be filled or empty. This is also true in a more general setting. Consider a system with $2N$ MZMs. All possible states of the system can then only be described by

pairing up the MZMs in a definite way and investigate for each pair if it is empty or filled. A different pairing would correspond to describing the system in a different basis.

This suggests the following, very general, picture. When two anyons are brought together, they form a new anyon. This process is called fusion. All fusion processes are given by the fusion rules which can be described by category theory. In this framework, the fusion rules can be described by

$$S_i \otimes S_j \simeq \bigoplus_k N_{ij}^k S_k. \quad (1.17)$$

Here \simeq means that the LHS and RHS are isomorphic as objects of a modular tensor category. The charges¹ of the anyons are represented by the S_i which are simple objects of this category. The numbers N_{ij}^k are called the fusion coefficients.[13]

This formula has a simple interpretation. Given two anyons with charge S_i and S_j , fusing them can have different resulting anyons S_k . The number of ways it can fuse to an anyon with charge S_k is given by the fusion coefficient N_{ij}^k .

For MZMs, the fusion rules are much simpler. There are only three possible charges. There is the vacuum charge $\mathbf{1}$, the charge of an electron ϵ and finally the charge of the MZM σ . There are the following fusion rules [14]

$$\epsilon \otimes \epsilon \simeq \mathbf{1}, \epsilon \otimes \sigma \simeq \sigma, \sigma \otimes \sigma \simeq \mathbf{1} \oplus \epsilon. \quad (1.18)$$

These rules can be interpreted as two electrons together becoming a Cooper pair and two MZMs that together are either empty or filled.

The use of category theory and fusion is not necessary for systems with Majorana zero modes. These systems are simple enough to be described by linear algebra and giving the state relative to some basis of pairings of the MZMs. As particle number is not conserved whenever fusion processes are considered, using only the braid group \mathcal{B}_n for a single value of n is not sufficient, all braid groups \mathcal{B}_n have to be considered simultaneously. For all groups a representation must be chosen that is compatible with the other braid groups and fusion. This is where category theory can help to ensure consistency [15].

1.4 Quantum computation with Majorana zero modes

A pair of MZMs can be in two states. Fusing them can either result in vacuum or in an electron. This means that two MZMs together are a 2 state system and therefore could form the basis of a qubit. The result of a fusion process only depends on the braiding of the two MZMs protecting the state of the qubit. The qubit does not couple to its noisy environment making the qubit more stable against decoherence.

In physical systems, the electron parity (i.e. the parity of the number of electrons) is conserved. This means that it is not possible to create a qubit with only two MZMs. If those two MZMs would have been created from the vacuum, they must always fuse to vacuum again to conserve parity. By constructing qubits from four MZMs, one pair can compensate for the parity of the other pair. The four possible states of a qubit are then $|00\rangle$, $|11\rangle$ for the even parity

¹The *charge* of an anyon is a label of the particle that denotes the type of anyon under consideration. This charge is not related to the electrical charge of the particles.

subspace and $|01\rangle, |10\rangle$ for the odd parity subspace. The first/second number denotes the result of fusion of the first/second MZM pair. The first MZM pair is associated with the fermion operator c_1 and the second pair with c_2 . The numbers then correspond to the fermion number operators $c_1^\dagger c_1$ and $c_2^\dagger c_2$.

If the qubit is in the even parity subspace, the state of the qubit is then given by:

$$|\psi\rangle = \alpha |00\rangle + \beta |11\rangle, \quad (1.19)$$

where $|\alpha|^2 + |\beta|^2 = 1$.

The result of braiding operations on the qubit can now be calculated. For example the braid

$$B_{23} = \left| \begin{array}{c} \text{---} \\ \text{---} \\ \text{---} \\ \text{---} \end{array} \right. \begin{array}{c} \text{---} \\ \text{---} \\ \text{---} \\ \text{---} \end{array} \left. \begin{array}{c} \text{---} \\ \text{---} \\ \text{---} \\ \text{---} \end{array} \right| \quad (1.20)$$

acts via $\rho(B_{23})$ on the state $|00\rangle$ as²

$$\begin{aligned} \rho(B_{23}) |00\rangle &= e^{\pi\lambda\gamma_2\gamma_3/4} |00\rangle = \frac{1}{\sqrt{2}}(1 + \lambda\gamma_2\gamma_3) |00\rangle = \\ &= \frac{1}{\sqrt{2}}(1 + \imath(c_1^\dagger - c_1)(c_2^\dagger + c_2)) |00\rangle = \frac{1}{\sqrt{2}}(|00\rangle + \imath |11\rangle). \end{aligned} \quad (1.21)$$

All other braid operations can be calculated similarly.

Unfortunately, the braid structure of Majorana qubits is not rich enough to support universal quantum computation. The $\pi/8$ gate is not possible with braiding of MZMs, also the CNOT gate is not possible within the logical subspace of the qubit. To resolve this problem, the topological gates must be complemented with non-topological gates [16]. Theoretical predictions have been made for other types of anyons which would allow topological universal quantum computing such as the *Fibonacci anyon* [15]. These ideas will however not be discussed in this thesis.

Several proposals aim to implement a Majorana qubit. The major difficulty when trying to implement these qubits is being able to move the MZMs such that they can be braided. Networks of nanowires have been proposed in which the MZMs are dragged around and can hence be braided [17].

A different proposal uses superconducting transmon qubits as a basis for Majorana qubits. The transmon is coupled to the fermion parity of the MZMs. The coupling can however be tuned exponentially by changing the E_J/E_C ratio of the transmon. Therefore the topological protection of the resulting *top-transmon* can be turned on and off. In the non-protected state, the qubit can be read-out and the $\pi/8$ and CNOT gate can be applied [18]. Changing the coupling between the MZMs leads to an effective braiding [19]. The non-abelian behavior of Majorana zero modes could be experimentally confirmed by building a suitable network of nanowires and superconducting islands [20]. In reference [20] they envision a setup as in Fig. 1.1. The effective Hamiltonian for the braiding operation is given by

$$H = -\imath\Delta_1\gamma_1'\gamma_3 - \imath\Delta_2\gamma_3\gamma_3' - \imath\Delta_3\gamma_3\gamma_2. \quad (1.22)$$

²Elements of groups can only act on states in the Hilbert space via a representation. The representation corresponding to the exchange of Majorana zero modes is denoted here by ρ .

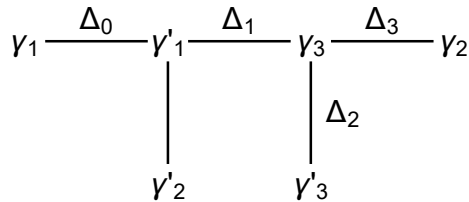


Figure 1.1: The experimental setup of the braiding experiment. Image adapted from [20].

Here, Δ_i denotes the coupling between Majorana pairs and can be tuned exponentially by changing the magnetic flux through the split Josephson junctions.

The result of the braiding operation can be obtained by solving the time dependent Schrödinger equation with the Hamiltonian of Eq. (1.22) using time dependent couplings Δ_i . The result of this simulation is shown in Fig. 1.2. Only the even parity subspace of the Hilbert space is used. Therefore only the even parity states are shown. In this braiding scheme, an extra ancillary Majorana pair is needed. Therefore the states are denoted with three quantum numbers. The states hence look like $|n_1 n_2 n_3\rangle$ where n_i is the occupation number of the fermion given by $\frac{1}{2}(\gamma'_i + v\gamma_i)$. Applying the braiding scheme repeatedly to the initial state $|000\rangle$ gives the following cycle:

$$\begin{aligned}
 |000\rangle &\mapsto \frac{1}{\sqrt{2}}(c_1 |000\rangle + c_2 |110\rangle) \mapsto \\
 &|110\rangle \mapsto \frac{1}{\sqrt{2}}(c_3 |000\rangle + c_4 |110\rangle) \mapsto |000\rangle. \quad (1.23)
 \end{aligned}$$

Here c_i denote relative phase factors obeying $|c_i|^2 = 1$.

1.5 Experimental realization of Majorana zero modes

In Sec. 1.2, MZMs were predicted to exist in an idealized model. The goal of this section is to translate the idealized requirements into physically realizable features. The idealized model contains a 1-dimensional superconducting nanowire which is effectively spinless. It is not immediately clear that such systems can be made in practice.

It is possible to create nanowires which are very thin compared to their length. The wires are long enough that the longitudinal quantization can be ignored. The orthogonal quantization induces large energy differences between the consecutive bands. This allows the system to effectively be described by a 1-dimensional model.

Normal, s-wave superconductors pair electrons of opposite spins into Cooper pairs. If the system is effectively spinless, it is not clear how to construct superconducting pairing. To overcome this problem spin orbit coupling will be used together with an magnetic field. It will be shown that these two ingredients can be combined to obtain spinless superconductivity. Spin orbit coupling leads to a term in the Hamiltonian that lifts the degeneracy of the two spin directions by an energy proportional to the momentum.

Calculations on the spin-orbit coupling will form the major part of this thesis. For the present purposes however, it is enough to consider spin-orbit coupling

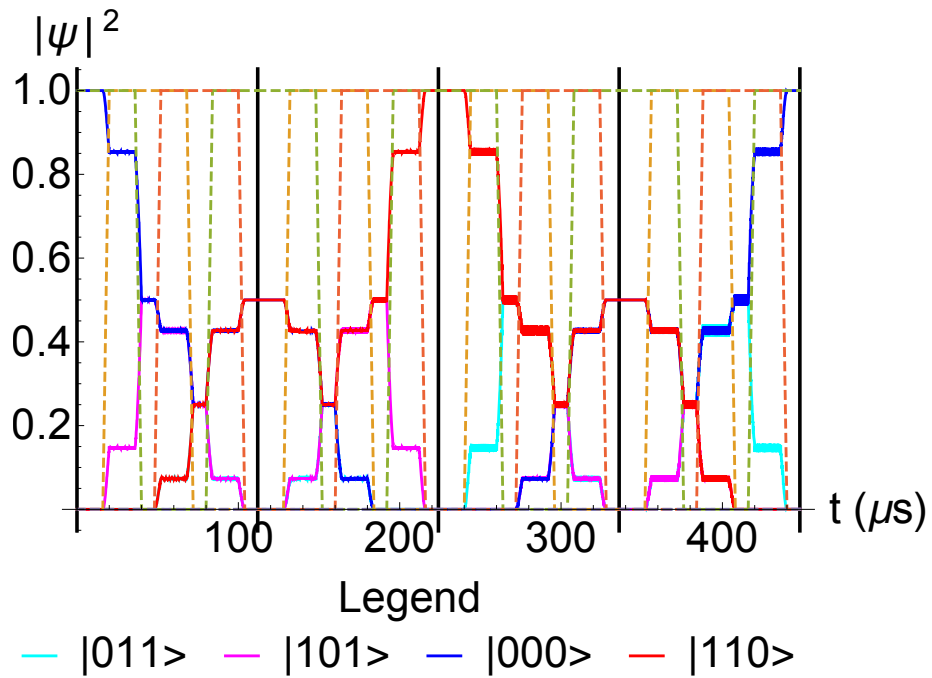


Figure 1.2: This figure shows the result of four consecutive virtual braiding operations. Each braiding operation is delimited by a black vertical line. The four solid lines denote the occupation probability of the four states in this calculation. The dashed lines represent the coupling Δ between the Majorana zero modes. This parameter depends on the magnetic flux through the split Josephson junctions. The horizontal axis denotes time in microseconds. This figure shows that each braiding operation cycles through the states of Eq. (1.23). The parameters for this simulation are $E_J = 2 \times 100$ GHz, $E_c = 0.5$ GHz and $E_m = 50$ GHz.

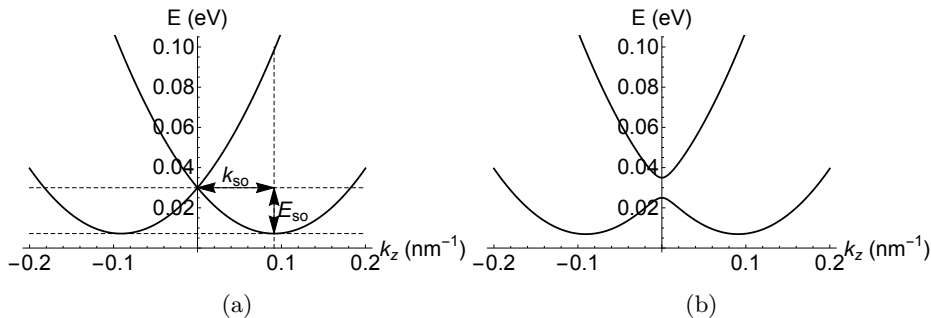


Figure 1.3: The band structure corresponding to the Hamiltonian in Eq. (1.24) **Fig. a** shows the band structure for $B_z = 0$, the definitions of E_{so} and k_{so} are given in this figure as well. **Fig. b** shows the band structure for a finite value of B_z . A gap opens when a finite magnetic field is introduced in the system.

as an effective term in the Hamiltonian proportional to $k_z \sigma_z$. The strength of the spin-orbit coupling is denoted by α (which depends on the electric field). Without a magnetic field this produces a band structure as in Fig. 1.3a. In this figure, the definition of k_{so} and E_{so} are shown as well. These quantities allow the spin-orbit strength to be calculated for simulated systems.

In order to obtain a system that can host Majorana zero modes, a magnetic field has to be added as well. This will produce the Hamiltonian

$$H = \frac{\hbar^2 k_z^2}{2m} - \mu + \alpha k_z \sigma_y + \frac{1}{2} g \mu_B B_z \sigma_z. \quad (1.24)$$

With g the Landé g-factor and μ_b the magnetic dipole moment. The band structure for a finite value of the magnetic field is shown in Fig. 1.3b.

If the chemical potential is low enough, only the lowest band in Fig. 1.3b is occupied, rendering the system is effectively spinless. Without spin-orbit interaction, only a single spin direction would be present in the system such that superconductivity cannot be induced. With spin-orbit interaction, both spin directions are still present in the system and superconductivity can be induced by coupling electrons of opposite spin and momentum.

In summary, there are four requirements for MZMs to appear:

- a 1-dimensional system
- a parallel magnetic field
- induced superconductivity
- strong spin-orbit interaction

This thesis will focus on the fourth requirement. Both theoretical results and simulations will be employed to predict the strength of the Rashba spin-orbit interaction in nanowires.

1.6 Thesis outline

The aim of this thesis is roughly twofold. Firstly to calculate the Rashba spin-orbit interaction in realistic nanowire systems and secondly to develop a

theory to independently check the numerical results and investigate the nanowire systems in a broader parameter regime.

In this chapter the basic properties of Majorana zero modes have been investigated and the major concepts of this thesis have been introduced. Here, the structure of the remainder of the thesis is described.

Chapter 2 presents a theoretical framework as a foundation for developing an analytical formula to predict the strength of Rashba spin-orbit interaction. This formula is then calculated in Chapter 3 together with a general Hamiltonian for semiconductors. The so called 8×8 Kane Hamiltonian.

The Kane Hamiltonian is then used to perform simulations in 2-dimensional quantum wells in Chapter 4. These simulations serve to introduce an intuition for the effects that emerge in this thesis. First, calculations are performed in reciprocal space, followed by real space calculations.

Finally, in Chapter 5, nanowires are simulated in a real space basis. First, a number of parameters like shape, width and growth direction are investigated. Then a Schrödinger-Poisson solver is used to induce a realistic electric field in these nanowires. The geometry used is similar to the device where the first signatures of MZMs were observed.

The contents of Chapter 1 is mainly based on existing literature. Only the simulation corresponding to Fig. 1.2 were performed by the author. Chapter 2 is also based on literature. Section 2.1 consists of well known definitions of representation theory. Sections 2.2 and 2.3 consist of examples of the preceding section. Finally, Sec. 2.4 is based on reference [21], but was fully rewritten. The author hopes that this section is easier to understand than the original. An effort was made to exclude as much dependencies as possible and arrive at a self contained proof of the theory of invariants.

Chapter 3 is mainly based on existing literature, but the results were re-derived by the author revealing a difference in the resulting formula in Eq. (3.39). Section 3.5 contains the explicit application of the theory to 1-dimensional nanowire systems. Here it was found that the existing theory leads to ambiguous results, which is resolved in this section by the author. Finally, Sec. 3.6 contains results that originated in discussions with Roland Winkler and Michael Wimmer which cannot be found in existing literature as far as the author is aware.

The results of Chapter 4 are calculated by the author using *Mathematica*. The results of Chapter 5 were also calculated by the author using *Kwant*. The Hamiltonian was implemented by Rafał Skolasiński. The Schrödinger-Poisson solver was implemented by Adriaan Vuik [22].

2 Symmetry

2.1 Representation theory

Representations of groups allow to study the behavior of groups in the context of linear algebra. Quantum mechanics can be formulated in the language of linear algebra making representations an important link between quantum mechanics and symmetry. This section is an attempt to capture the most important aspects of representations for this thesis. First, representations will be defined together with some important properties. Afterwards the concept of restrictions and characters will be enlightened.

Let G be a group and V be a vector space. The group of linear maps on V is denoted as $\text{GL}(V)$. A representation is a group homomorphism ρ between G and $\text{GL}(V)$. The complete definition of ρ is then

$$\rho : G \rightarrow \text{GL}(V) : g \mapsto \rho(g) \text{ such that } \forall g, h \in G : \rho(gh) = \rho(g)\rho(h). \quad (2.1)$$

The dimension n of V is called the dimension of the representation ρ .

If a representation maps only to unitary matrices, the representation is said to be unitary. This condition can be expressed as

$$\rho^\dagger(g) = \rho^{-1}(g). \quad (2.2)$$

If the vector space has a nonempty subspace $W \subsetneq V$ such that

$$\forall g \in G, w \in W : \rho(g)w \in W, \quad (2.3)$$

then ρ is said to be reducible. If no such subspace exists, ρ is said to be irreducible. Note that for a 1-dimensional representation, such a subspace cannot exist. Hence, a 1-dimensional representation is always irreducible.

Because representations which are both unitary and irreducible will play an important part in the rest of this thesis, *unitary irreducible representation* is abbreviated to *unirrep*.

It is possible to define a basis on our vector space V of vectors e_1, \dots, e_n . Any vector $v \in V$ can be denoted in terms of this basis, $v = \sum_i v_i e_i$. Then $\rho(g)$ can be thought of as a matrix, with components $\rho(g)_{ij}$, acting on the components of the vectors. Instead of letting $\rho(g)$ act on the components of a vector, $\rho(g)$ can also act on the basis of the vector space itself. In other words, the vector components no longer transforming according to

$$v_i \mapsto \sum_j \rho(g)_{ij} v_j, \quad (2.4)$$

but instead the basis vectors themselves transform according to

$$e_j \mapsto \sum_i e_i \rho(g)_{ij}. \quad (2.5)$$

Note that the vector v gets mapped to the same physical vector in both notations. A set of basis vectors which transform according to Eq. (2.5) is called a basis of a representation ρ .

Given two representations ρ from G to $\text{GL}(V_\rho)$ and σ from G to $\text{GL}(V_\sigma)$ these representations can be combined to form new representations. First define the direct sum of two representations as

$$(\rho \oplus \sigma)(g) = \rho(g) \oplus \sigma(g). \quad (2.6)$$

The direct sum on the RHS must be understood as the direct sum of matrices. It can be shown that $\rho \oplus \sigma$ is again a representation from G to $\text{GL}(V_\rho \oplus V_\sigma)$. Similarly the (Kronecker) product [23] of two representations can be defined as

$$(\rho \otimes \sigma)(g)_{ik,jl} = (\rho(g) \otimes \sigma(g))_{ik,jl} = \rho(g)_{ij} \sigma(g)_{kl}. \quad (2.7)$$

It can again be checked that this is a genuine representation from G to $\text{GL}(V_\rho \otimes V_\sigma)$. Finally one can take the complex conjugate of a representation by

$$\rho^*(g) = \rho(g)^*, \quad (2.8)$$

which is again a representation.

The character of a representation is defined as

$$\chi_\rho : G \rightarrow \mathbb{C} : g \mapsto \text{Tr}(\rho(g)). \quad (2.9)$$

In general, a character can map to an arbitrary field. In this thesis this will always be the complex numbers however. An important property of characters is that it maps the identity to the dimension of the representation,

$$\chi_\rho(e) = n. \quad (2.10)$$

Furthermore, there exist the following identities for the composition of characters which can be proved using the definitions for the respective representations.

$$\chi_{\rho \oplus \sigma} = \chi_\rho + \chi_\sigma \quad (2.11)$$

$$\chi_{\rho \otimes \sigma} = \chi_\rho \cdot \chi_\sigma \quad (2.12)$$

$$\chi_{\rho^*} = \overline{\chi_\rho} \quad (2.13)$$

Using characters it can be shown that any reducible representation can be reduced into the direct sum of irreducible constituents. Hence a reducible representation ρ can be written as

$$\rho = \bigoplus_{i \in I} \rho_i^{a_i}, \quad (2.14)$$

where the direct sum is indexed by the irreducible representations ρ_i . The number of times that a representation ρ_i is contained in ρ is given by the number a_i . This number can be determined by [24]

$$a_i = \frac{1}{h} \sum_{g \in G} [\chi_{\rho_i}(g)]^* \chi_\rho(g), \quad (2.15)$$

where h is the order of the group G under consideration.

Once the irreducible representations of a group G are known, it is interesting to look at representations in a subgroup $H < G$. If an irreducible representation is restricted from G to H , then the resulting representation might be

reducible. This restricted representation can then be decomposed into the sum of irreducible representations. This decomposition is encoded in the so called branching laws [25].

In the next subsections two examples will be discussed before continuing with the implications of symmetry. These examples are very different in nature, but very similar in framework. The first example considers the structure of spin. It is shown that bosonic spins correspond to irreducible representations of $SO(3)$ while fermionic spins appear only when the more complete structure of $SU(2)$ is studied.

The second example has the same structure, but considers exchange statistics. By studying the permutation group, normal bosonic and fermionic exchange statistics are recovered. To recover anyonic exchange statistics, the more complete braid group has to be studied.

2.2 Application of symmetry to spin

In this section the symmetry properties of spin will be considered. Spin is an important property of particles in quantum mechanics that describes intrinsic angular momentum. By considering the 3-dimensional rotation group, the integer spin particles appear as irreducible representations. By studying the universal cover group of the rotation group, half-integer spin representations will appear as well.

Consider rotation of space. These rotations can be described by group theory. The group containing all rotations in 3-dimensional space is isomorphic to $SO(3)$, the special orthogonal group in three dimensions. The group $SO(3)$ contains all 3-dimensional real orthogonal matrices with unit determinant. This can be written as

$$SO(3) = \{M \in GL(\mathbb{R}^3) | M^T = M^{-1}, \det(M) = 1\}. \quad (2.16)$$

This group allows for an infinite number of irreducible representations. These representations all have an odd number of dimensions [26] and correspond to particles with integer spin. Hence the transformation rules for bosons are recovered, but fermions do not fit into these representations.

The problem is that the description of rotation by $SO(3)$ is not faithful as the group $SO(3)$ is not simply connected. This means that a closed path of rotations can not always be contracted to a point. Starting with the identity and rotating along an arbitrary axis by 2π yields the identity rotation, but the path cannot be contracted to a point. Only by rotating by 2π once more, the path can be contracted to a point again.

This can be visualized by representing rotations as $\hat{n}\phi$ with \hat{n} a unit vector and ϕ the angle of rotation around this unit vector. The space of all rotations is then a ball with radius π that has the antipodal points identified which is called the *parametric ball* [23]. A path of a rotation by 2π can be represented by a path going from the center of the parametric ball to the south pole which is identified to the north pole from which the path goes down further to the center. This path cannot be deformed to a point, but a path corresponding to a rotation of 4π can be deformed to a point which is shown in Fig. 2.1.

This means that Quantum mechanics can (and sometimes will) make a difference between a rotation of 2π and 4π . Therefore a group is needed to take

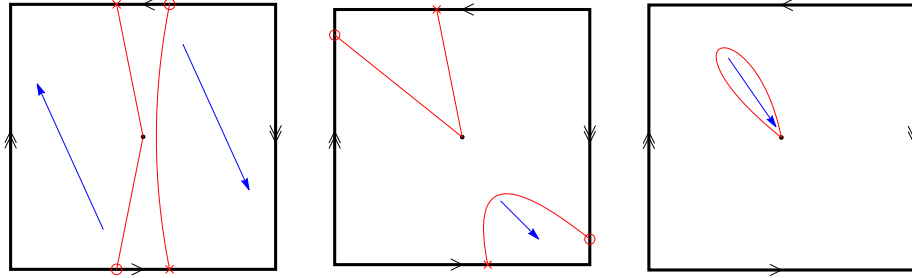


Figure 2.1: A rotation of 4π is shown by a red line in a cross section of the parametric ball, which is represented by a square with opposite ends identified. By deforming the path along the blue arrows, the path can be deformed to a point.

this additional structure into account. This group is called $SU(2)$ and is isomorphic to the group of equivalence classes of homotopic paths³ in $SO(3)$. Hence the special unitary group has to be used when describing rotations. This group is described by

$$SU(2) = \{M \in GL(\mathbb{C}^2) | M^\dagger = M^{-1}, \det(M) = 1\}. \quad (2.17)$$

The groups $SO(3)$ and $SU(2)$ are connected by a group homomorphism such that the irreducible representations in $SO(3)$ can be lifted to an irreducible representation of $SU(2)$. This group homomorphism is denoted by $\phi : SU(2) \rightarrow SO(3)$ and is a double cover⁴, hence ϕ is *onto*. The kernel of ϕ is $\{\pm I\} \simeq \mathbb{Z}_2$, hence the isomorphism theorem gives [26]

$$SU(2)/\mathbb{Z}_2 \simeq SO(3). \quad (2.18)$$

Given an irreducible representation ρ of $SO(3)$, $\rho \circ \phi$ gives an irreducible representation on $SU(2)$.

It is possible to define all finite dimensional representations on $SU(2)$. Define the representation π_n on $SU(2)$ acting on the space of homogeneous polynomials $P(z_1, z_2)$ of degree n by

$$\pi_n(g)P\left(\begin{pmatrix} z_1 \\ z_2 \end{pmatrix}\right) = P(g^{-1}\begin{pmatrix} z_1 \\ z_2 \end{pmatrix}), \quad (2.19)$$

where g must be thought of as a two dimensional matrix and P is a homogeneous polynomial on z_1 and z_2 of degree n . Note that the representation π_n has dimension $n + 1$. It can be proven that all irreducible representations of $SU(2)$ are equivalent to one of the representations π_n [26]. The representations that are lifted from $SO(3)$ to $SU(2)$ correspond to all π_n with even n . These are all odd dimensional representations corresponding to integer spin and obey

$$\rho(\theta\vec{n}) = \rho((\theta + 2\pi)\vec{n}). \quad (2.20)$$

³Two paths are homotopic if they can be continuously deformed in one another.

⁴A double cover means that for each element in $SO(3)$ there are exactly 2 elements in $SU(2)$ that get mapped to it.

For odd n , the representations π_n has no counterpart in $\text{SO}(3)$. These representations have odd dimension and correspond to half-integer spin. These fermionic representations obey

$$\rho(\theta\vec{n}) = -\rho((\theta + 2\pi)\vec{n}). \quad (2.21)$$

Electrons are particles with spin $1/2$. Hence they are fermions and as discussed in the introduction do not return to themselves after a rotation of 2π . The representation of electrons is denoted by $D_{\frac{1}{2}}$. This representation will play an important role in the symmetry considerations of Chapter 3.

2.3 Application of symmetry to exchange statistics

Exchange statistics are the basis for very important properties of quantum mechanical systems. The symmetry of bosons allows them to condense in a Bose-Einstein condensate. The anti-symmetry of fermions gives rise to the Pauli exclusion principle. This section will show how these statistics arise from the permutation group. Next, the braid group is considered to study anyonic exchange statistics. To describe the exchange statistics, representation theory is used as a framework. This exposes the difference between anyons, fermions and bosons.

The symmetry of the exchange of particles is described by the permutation group. The permutation group S_n on n particles can be built by considering the $n - 1$ pairwise exchange operators σ_i that exchanges particles i and $i + 1$. These operators obey the following relations:

$$\sigma_i\sigma_j = \sigma_j\sigma_i \text{ for } |i - j| \neq 1 \quad (2.22)$$

$$\sigma_i\sigma_{i+1}\sigma_i = \sigma_{i+1}\sigma_i\sigma_{i+1} \quad (2.23)$$

$$\sigma_i^2 = 1. \quad (2.24)$$

This group has two 1-dimensional unirreps for $n \geq 2$. The first is the trivial representation which sends every element to the 1-dimensional identity matrix. The second is the alternating representation which sends the group elements σ_i to minus the identity. This uniquely defines the representation on the other elements as well. These two representations correspond to bosons and fermions respectively. These are the only 1-dimensional unirreps as can be seen by considering $\sigma_i^2 = 1$. This means that for any unirrep ρ it holds that $\rho(\sigma_i) = \pm 1$. If $\rho(\sigma_i) = \pm 1$ for a certain i then by Eq. (2.23), $\rho(\sigma_j)$ has the same sign for all j . This leads to the trivial and alternating representation of the permutation group.

Similar to the fact that $\text{SO}(3)$ gives an incomplete picture of spin (see Sec. 2.2), S_n gives an incomplete picture of the symmetry of particle exchange. In other words, the description of the exchange process given by the permutation group is not faithful. For spin, the paths traversed in $\text{SO}(3)$ by the particles must be taken into account. Similarly for exchange statistics, it is necessary to take the paths traversed in configuration space into account. The group taking the history of exchanges into account is given by the braid group \mathcal{B}_n . The braid group looks a lot like the permutation group with the exception that Eq. (2.24)

⁵There are also higher dimensional irreducible representations of the permutation group. These representations lead to parastatistics [27]. A discussion of parastatistics would lead us beyond the scope of this thesis.

is dropped as a relation. Hence, the definition of the braid group is given by the generators $\sigma_1 \dots \sigma_{N-1}$ and the relations:

$$\sigma_i \sigma_j = \sigma_j \sigma_i \text{ for } |i - j| \neq 1 \quad (2.25)$$

$$\sigma_i \sigma_{i+1} \sigma_i = \sigma_{i+1} \sigma_i \sigma_{i+1}. \quad (2.26)$$

A 1-dimensional unirrep of the braid group can assign any phase to the braiding of two particles

$$\rho(\sigma_i) = e^{i\theta}. \quad (2.27)$$

Particles that have exchange statistics according to this representation are called (abelian) anyons. The braid group contains the permutation group as a subgroup. The representations for bosons and fermions can be recovered for $\theta = 0$ and $\theta = \pi$ respectively. Hence, bosons and fermions can be thought of as special cases of a more comprehensive set of representations.

There are also higher dimensional representations of the braid group. In these representations it might happen that

$$\rho(g_1)\rho(g_2) \neq \rho(g_2)\rho(g_1). \quad (2.28)$$

If this is the case, the exchange statistics are said to be non-abelian.

A group homomorphism $\phi : S_n \rightarrow \mathcal{B}_n$ can be constructed by mapping a braid to the corresponding exchange of strands, but neglecting the intermediate exchanges. The kernel of this homomorphism gives rise to a subgroup of \mathcal{B}_n which is called the pure braid group \mathcal{P}_n . This group consists of all braids where the final position of all strands is the same as their initial position. By the isomorphism theorem [26]

$$\mathcal{B}_n/\mathcal{P}_n \simeq S_n. \quad (2.29)$$

In (3+1) dimensional systems it is possible to continuously deform any braid in the pure braid group to the identity braid [27]. Therefore, only the permutation group is needed to describe particle exchange. In contrast for a lower number of dimensions, this deformation is not possible which can lead to anyons emerging in these systems.

2.4 Symmetry and the theory of invariants

The goal of this section is to describe the conditions that are imposed on the Hamiltonian by symmetry considerations. This method was first described by Bir and Pikus in reference [21]. This section aims to explain the theory of invariants using only basic representation theory.

The Hamiltonian is an operator in the state space. It generally depends on a variety of physical fields, such as the electric and magnetic field but also the momentum operators. These fields are denoted by a general tensor \mathcal{K} leading to $\mathcal{H}(\mathcal{K})$. The explicit form of the Hamiltonian depends on the basis of the fields and the state space. If the system is invariant under a certain group of symmetry operations, then the Hamiltonian must obey the same symmetries. That means that the Hamiltonian should be invariant under a symmetry transformation on the basis vectors of the state space and a simultaneous transformation of the physical fields.

Consider a representation ρ of the symmetry group G in the state space with basis e_1, \dots, e_n . The Hamiltonian can then be written relative to this basis. The matrix elements are

$$\mathcal{H}_{ij} = \langle e_i | \mathcal{H} | e_j \rangle. \quad (2.30)$$

It is known how the basis transforms under elements of G . This can be used to determine how the matrix \mathcal{H} changes under transformations of the basis vectors.

$$\mathcal{H}_{ij} \mapsto \mathcal{H}'_{ij} = \left\langle \sum_k e_k \rho(g)_{ki} \middle| \mathcal{H} \middle| \sum_p e_p \rho(g)_{pj} \right\rangle = \sum_{kp} \langle e_k \rho(g)_{ki} | \mathcal{H} | e_p \rho(g)_{pj} \rangle. \quad (2.31)$$

Using the fact that $\rho(g)_{ki}$ and $\rho(g)_{pj}$ are just complex numbers, ρ is a unitary representation and the definition of \mathcal{H}_{kp} it is possible to rewrite this expression to

$$\mathcal{H}'_{ij} = \sum_{kp} \rho(g)_{ki}^* \langle e_k | \mathcal{H} | e_p \rangle \rho(g)_{pj} = \rho(g)_{ik}^{-1} \mathcal{H}_{kp} \rho(g)_{pj}. \quad (2.32)$$

The transformation of the fields by a symmetry operation is denoted by \hat{g} . Then the invariance of the systems gives

$$\rho(g)^{-1} \mathcal{H}(\hat{g}\mathcal{K}) \rho(g) = \mathcal{H}(\mathcal{K}). \quad (2.33)$$

This can be rewritten to the central equation of this section

$$\rho(g) \mathcal{H}(g^{-1}\mathcal{K}) \rho(g)^{-1} = \mathcal{H}(\mathcal{K}). \quad (2.34)$$

This equation must hold for all elements of the symmetry group G and captures the constraints posed by symmetry on the Hamiltonian. However, this condition does not immediately show how to construct Hamiltonians that satisfy this constraint. A flaw that is remedied by the theory of invariants. This theory shows that the Hamiltonian must be the sum of so called invariants. How these invariants arise will be the subject of the remainder of this section.

Eq. (2.34) in this compact form is not useful in order to make progress. The symmetry structure of the matrix \mathcal{H} and the tensor \mathcal{K} are not explicitly present in the equation. Expanding \mathcal{H} and \mathcal{K} in turn in a suitable basis solves this problem.

Firstly, a suitable basis for \mathcal{H} must be formed. Such a basis consists of n^2 matrices of dimensions $n \times n$. It is possible to construct these n^2 basis elements, X_i , such that X_i does not depend on \mathcal{K} . In order to express the Hamiltonian in these basis elements, n^2 functions $f_i : \mathcal{K} \mapsto f(\mathcal{K}) \in \mathbb{C}$ need to be found such that

$$\mathcal{H}(\mathcal{K}) = \sum_i f_i(\mathcal{K}) X_i. \quad (2.35)$$

A representation can then be defined by

$$X_i \mapsto X'_i = \rho(g) X_i \rho(g)^{-1}. \quad (2.36)$$

The matrices X_i form a basis for all $n \times n$ matrices, which ensures that an explicit formulation of this representation can be found in the form of a matrix $\rho^X(g)_{ji}$ such that

$$X'_i = \sum_j X_j \rho^X(g)_{ji}. \quad (2.37)$$

In order for ρ^X to be a representation, it must be shown that it behaves as a group homomorphism,

$$\rho^X(gh) = \rho^X(g)\rho^X(h). \quad (2.38)$$

This result follows by substituting the definition of ρ^X and using that ρ is itself a representation,

$$X_j \rho_{ji}^X(gh) = \rho(gh) X_i \rho(gh)^{-1} = \rho(g) \rho(h) X_i \rho(h)^{-1} \rho(g)^{-1}. \quad (2.39)$$

Substituting back the definition of ρ^X gives

$$X_j \rho_{ji}^X(gh) = \rho(g) X_k \rho^X(h)_{ki} \rho(g)^{-1} = X_j \rho^X(g)_{jk} \rho^X(h)_{ki}. \quad (2.40)$$

Hence, ρ^X is a representation and the X_i form a basis for this representation. This representation is in general reducible. This representation can be decomposed into its irreducible constituents indexed by μ . This gives a new set of representations ρ^μ and basis matrices X_i^μ ,

$$X_i^\mu \mapsto \rho(g) X_i^\mu \rho(g)^{-1} = \sum_j X_j^\mu \rho^\mu(g)_{ji}. \quad (2.41)$$

Therefore Eq. (2.35) becomes

$$\mathcal{H}(\mathcal{K}) = \sum_{i\mu} f_i^\mu(\mathcal{K}) X_i^\mu. \quad (2.42)$$

The matrices X_i^μ make it possible to make a first step rewriting Eq. (2.34),

$$\mathcal{H} = \rho(g) \sum_{i\mu} f_i^\mu(g^{-1}\mathcal{K}) X_i^\mu \rho(g)^{-1} = \sum_{i\mu} f_i^\mu(g^{-1}\mathcal{K}) \rho(g) X_i^\mu \rho(g)^{-1}. \quad (2.43)$$

Hence,

$$\mathcal{H} = \sum_{i\mu} f_i^\mu(\mathcal{K}) X_i^\mu = \sum_{ij\mu} f_i^\mu(g^{-1}\mathcal{K}) X_j^\mu \rho^\mu(g)_{ji}. \quad (2.44)$$

Using that the X_i^μ form a basis, the factors in front of these matrices can be equated

$$f_l^\mu(\mathcal{K}) = \sum_i f_i^\mu(g^{-1}\mathcal{K}) \rho^\mu(g)_{li}. \quad (2.45)$$

Now, a suitable basis for \mathcal{K} will be constructed. The existence of this basis guarantees that $g^{-1}\mathcal{K}$ can be expanded in this basis. The fields in \mathcal{K} transform as vectors. In other words, they obey the following transformation rule

$$\mathcal{K}'_i = g^{-1}\mathcal{K} = \rho^\mathcal{K}(g^{-1})_{ij} \mathcal{K}_j. \quad (2.46)$$

This can be split in irreducible components labeled by λ and rewritten to

$$\mathcal{K}'_j^{\lambda^*} = \sum_k \rho_{kj}^{\lambda^*}(g) \mathcal{K}_k^{\lambda^*}. \quad (2.47)$$

The functions f_i^μ must now be expanded in the basis of \mathcal{K} . The coefficients of this expansion depend on the indices of the function f and on all the indices

of the basis of \mathcal{K} . Hence, the coefficients are complex numbers denoted by $c_{kj}^{\mu\lambda}$. Then the explicit expansion looks like

$$f_k^\mu = \sum_{j\lambda} c_{kj}^{\mu\lambda} \mathcal{K}_j^{\lambda*}. \quad (2.48)$$

Substituting this into Eq. (2.45) yields

$$\sum_{j\lambda} c_{lj}^{\mu\lambda} \mathcal{K}_j^{\lambda*} = \sum_{im\lambda} \rho^\mu(g)_{li} c_{im}^{\mu\lambda} \mathcal{K}_m^{\lambda*}. \quad (2.49)$$

Now \mathcal{K}' can be expanded as

$$\sum_{j\lambda} c_{lj}^{\mu\lambda} \mathcal{K}_j^{\lambda*} = \sum_{imj\lambda} \rho^\mu(g)_{li} c_{im}^{\mu\lambda} \mathcal{K}_j^{\lambda*} \rho^{\lambda*}(g)_{jm}. \quad (2.50)$$

Using that the terms $\mathcal{K}_j^{\lambda*}$ form a basis leads to

$$c_{lj}^{\mu\lambda} = \sum_{im} \rho^\mu(g)_{li} c_{im}^{\mu\lambda} \rho^{\lambda*}(g)_{jm}. \quad (2.51)$$

This can be rewritten as

$$c_{lj}^{\mu\lambda} = \sum_{im} \left(\rho^\mu(g) \otimes \rho^{\lambda*}(g) \right)_{lj,im} c_{im}^{\mu\lambda}. \quad (2.52)$$

The tensor product of two representations is again a representation (cf. Eq. (2.7)). The equation above holds for all elements of the symmetry group. If c is interpreted as a vector with index im , then this representation has a one-dimensional invariant subspace, where it acts as the identity representation. The identity representation is only present in $\rho^\mu(g) \otimes \rho^{\lambda*}(g)$ if $\lambda = \mu$ [28].

Combining this with $\rho^{\lambda*}(g)_{ij} = \rho^\lambda(g^{-1})_{ji}$, the symmetry condition can be rewritten as

$$\sum_j c_{lj}^\mu \rho^\mu(g)_{jk} = \sum_i \rho^\mu(g)_{li} c_{ik}^\mu. \quad (2.53)$$

Interpreting c_{ij} as an operator, the equation tells us that c commutes with all elements of the representation. By Schur's second lemma [28] it follows that

$$c_{lm}^{\mu\lambda} = c^\mu \delta_\mu^\lambda \mathbb{1}_{lm} \quad (2.54)$$

where $c^\mu \in \mathbb{C}$ and no summation over μ is implied. This result leads to

$$\mathcal{H}(\mathcal{K}) = \sum_{i\mu j\lambda} c_{ij}^{\mu\lambda} \mathcal{K}_j^{\lambda*} X_i^\mu = \sum_\mu c^\mu \sum_i \mathcal{K}_i^{\mu*} X_i^\mu. \quad (2.55)$$

The terms in this equation are called invariants. It is important to notice that if the initial representation ρ is reducible, then ρ can be written as the direct sum of representations. Then in turn, the Hamiltonian can be factored into blocks. For each of these blocks the symmetry requirement can be written as

$$\rho^\alpha(g) \mathcal{H}_{\alpha\beta} (g^{-1} \mathcal{K}) \rho^\beta(g)^{-1} = \mathcal{H}_{\alpha\beta}. \quad (2.56)$$

This affects the theory of invariants by reducing Eq. (2.41) to

$$\rho^\alpha(g)_{ab} X_{bc}^{\mu i} \rho^\beta(g^{-1})_{cd} = \left(\rho^\alpha(g) \otimes \rho^{\beta^*}(g) \right)_{ad,bc} X_{bc}^{\mu i}. \quad (2.57)$$

This shows that the representation ρ^X must be contained in the representation $\rho^\alpha(g) \otimes \rho^{\beta^*}(g)$ meaning that all blocks of the Hamiltonian can only contain the invariants that transform according to the right representations which results in a huge restriction on the terms that are allowed in the Hamiltonian. The effects on the structure of the Hamiltonian are demonstrated in Sec. 3.3.

Finally it is worth mentioning that time reversal adds an additional requirement to the diagonal blocks in the Hamiltonian $\mathcal{H}_{\alpha\beta}$. Only the invariants that are invariant under time reversal are allowed as diagonal blocks.[29]

3 General semiconductor systems

3.1 Exposition of spin-orbit interaction

Spin-orbit interaction is an effect that couples momentum and spin through the electric field. The easiest way to understand this effect is to look at a semiclassical calculation of an electron in orbit around a nucleus. Assume that there are no external magnetic fields. In this situation there is only the electric field of the nucleus that needs to be considered. In the derivation, care is needed to keep the order of the operators because these do not generally commute. A figure depicting the situation under considerations is shown in Fig 3.1.

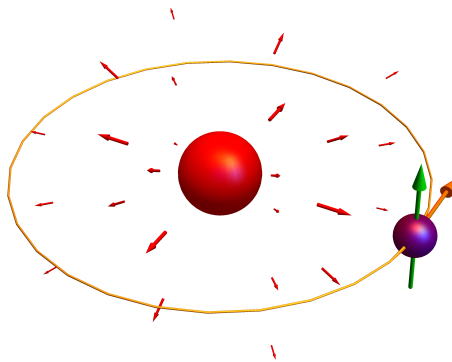


Figure 3.1: This figure is a cartoon of spin-orbit interaction of an electron around a nucleus. The nucleus is depicted in red, the electron in purple and the orbit in orange. The spin of the electron is indicated by a green arrow.

First, make a transformation to the inertial frame of the electron. The Lorentz transformation gives the magnetic field in this frame,

$$\vec{B}' = \gamma(\vec{B}_\perp - \frac{1}{c}\vec{\beta} \times \vec{E}). \quad (3.1)$$

Here, \vec{B} and \vec{E} denote the fields in the inertial frame of the nucleus, \vec{B}' denotes the magnetic field in the reference frame of the electron. Note that $\vec{p} = \gamma m \vec{v}$, hence, in the absence of an external magnetic field, \vec{B}' is given by

$$\vec{B}' = -\frac{1}{mc^2}\vec{p} \times \vec{E}. \quad (3.2)$$

This magnetic field couples to the spin of the electron via [30]

$$H_{\text{SO}} = -\vec{\mu} \cdot \vec{B}'. \quad (3.3)$$

For an electron, $\vec{\mu}$ is given by

$$\vec{\mu} = \frac{ge}{2m}\vec{S} \text{ with } \vec{S} = \frac{\hbar}{2}\vec{\sigma}. \quad (3.4)$$

Putting these formulas together gives

$$H_{\text{SO}} = \frac{(g-1)e}{2m^2c^2} \vec{S} \cdot (\vec{p} \times \vec{E}). \quad (3.5)$$

Here, 1 is subtracted from the g-factor to compensate for the fact that the electron is not in an inertial frame. By doing so, the Thomas precession is taken into account[31].

In the case of an electron around a nucleus, the electric field is spherically symmetric making it possible to write it as

$$\vec{E} = -\nabla\phi(r) = -\frac{\partial\phi}{\partial r} \hat{r} = -\frac{\vec{r}}{r} \frac{\partial\phi}{\partial r}. \quad (3.6)$$

When this field is substituted into the Hamiltonian, the new Hamiltonian becomes

$$H_{\text{SO}} = \frac{(g-1)e}{2m^2c^2} \vec{S} \cdot (\vec{p} \times \vec{r} \frac{1}{r} \frac{\partial\phi}{\partial r}). \quad (3.7)$$

To introduce the angular momentum operator $\vec{L} = \vec{r} \times \vec{p}$ the product in Eq. (3.7) has to be reversed. Doing this explicitly yields

$$(\vec{p} \times \vec{r})_i = \epsilon_{ijk} p_j r_k = \epsilon_{ijk} r_k p_j - \hbar \epsilon_{ijk} \delta_{jk} = -\epsilon_{ikj} r_k p_j = -(\vec{r} \times \vec{p})_i. \quad (3.8)$$

Now, the commutation relations of the electric field and the other terms in the equation will be investigated. Momentum operators do not generally commute with objects that depend on position. The angular momentum operator L_i however, does commute with spherical symmetric objects. Let $f(r)$ be a spherically symmetric function, then

$$[L_i, f(r)] = \sum_{j,k} \epsilon_{ijk} r_j p_k f(r) \propto \sum_{j,k} \epsilon_{ijk} \left(r_j \frac{\partial r}{\partial r_k} \right) \frac{\partial f}{\partial r} = 0. \quad (3.9)$$

This means that the electric field can be placed in front of $\vec{S} \cdot \vec{L}$. Plugging this all into Eq. (3.7) gives the spin-orbit Hamiltonian,

$$H_{\text{SO}} = -\frac{(g-1)e}{2m^2c^2} \frac{1}{r} \frac{\partial\phi}{\partial r} \vec{S} \cdot \vec{L}. \quad (3.10)$$

In mesoscopic systems a term similar to Eq. (3.5) also appears in the Hamiltonian. Only in the mesoscopic case, there is a different constant in front of the interaction. One could derive the spin-orbit splitting in semiconductors by considering only an external electric field applied to the system. This would however give results that are far weaker than the observed spin-orbit splittings. The reason for this is that in such a derivation, the strong electric fields of the nuclei in the system are neglected. The derivation of Rashba spin-orbit splitting will be the subject of the remainder of this chapter.

3.2 Broken symmetries and spin-orbit interaction

Symmetry plays a central role in the derivation of the Hamiltonian of this system. Therefore this section starts with some general symmetry considerations. A symmetry of nature is given by the CPT invariance [32]. A combination of

charge conjugation, parity transformation⁶ and time reversal. These transformations can give important restrictions on spin splitting.

This restriction can be obtained by considering parity transformation

$$\mathcal{P} : \vec{x} \mapsto -\vec{x}. \quad (3.11)$$

and time reversal

$$\mathcal{T} : t \mapsto -t. \quad (3.12)$$

If a system is symmetric under parity transformation, then the energy dispersion relation of the system obeys

$$E_{\vec{k}\uparrow} = E_{-\vec{k}\uparrow}. \quad (3.13)$$

The systems which are considered in this thesis are symmetric under time reversal. Time reversal symmetry holds long as no explicit time dependence is introduced in the Hamiltonian and there is no magnetic field. Time reversal reverses the direction of spin. Hence, systems symmetric under time reversal obey Kramers degeneracy [24],

$$E_{\vec{k}\uparrow} = E_{-\vec{k}\downarrow}. \quad (3.14)$$

These two energy relations can be combined in order to get

$$E_{\vec{k}\uparrow} = E_{\vec{k}\downarrow}. \quad (3.15)$$

This means that the energy of spin-up and spin-down particles in the system must be identical. Consequently there can be no spin splitting. In order to obtain a non-zero spin splitting, it is necessary to break the symmetry under parity transformation or time reversal.

Breaking time reversal symmetry can be done by applying an external magnetic field. This induces Zeeman spin splitting lifting the spin degeneracy. It is important to note however, that this splitting does not depend on momentum. In general, terms linear in magnetic field and momentum can be formed. In the diagonal blocks of the Hamiltonian however, all terms must be invariant under time reversal (see Sec. 2.4). A function linear in momentum, magnetic field and spin would be odd under time reversal and does therefore not contribute to spin-orbit splitting in the effective electron Hamiltonian [21].

There are two important ways in which parity transformation symmetry can be broken. The first is to break the microscopic parity transformation symmetry. zincblende and wurtzite structures do not have inversion symmetry, hence the spin degeneracy can be lifted. Dresselhaus spin-orbit splitting can result from this type of asymmetry. This type of parity asymmetry is called bulk inversion asymmetry (BIA) and will be briefly discussed in Sec. 3.6.

Another way to break parity transformation symmetry is to have structure inversion asymmetry (SIA). This means that parity is broken by an external field. The electric potential of an electric field generally depends on position and breaks parity inversion symmetry. Such an electric field couples the momentum and spin of an electron. This is called Rashba spin-orbit interaction. The Rashba effect will be investigated in the remainder of this thesis. How Rashba spin-orbit interaction arises in mesoscopic systems follows by performing a Löwdin partitioning on the multiband Hamiltonian that will be derived in Sec. 3.3.

⁶Note that parity transformation is unrelated to the fermion parity in a superconductor, although both are referred to as parity.

3.3 Semiconductor band structures: The Kane Hamiltonian

It is now interesting to see how a Hamiltonian can be formed for electrons and holes in a semiconductor. It turns out that if the theory of invariants is taken into account, it is possible to give an approximate Hamiltonian.

The relevant symmetry group in semiconductors is given by the group $SU(2)$ (see Sec. 2.2) together with the behavior under parity transformation. The resulting group is denoted by

$$\mathcal{R} = SU(2) \times C_i. \quad (3.16)$$

In this thesis we are only interested in the first conduction band of electrons and they have a central position in the Hamiltonian. The wavefunction of an electron has transformation properties derived from the full rotation group. It is important to find out how all the bands transform in the full rotation group. Electrons transform according to the irreducible representation $D_{\frac{1}{2}}^+$ of $SU(2)$. The lowest conduction band of zincblende structures is even with respect to parity. This means that the lowest conduction band transforms according to $D_{\frac{1}{2}}^+$. The representations of the highest valence bands can also be determined. The light and heavy holes transform according to $D_{\frac{3}{2}}^-$. The last band that will be taken into account is the spin splitoff band. These holes transform according to $D_{\frac{1}{2}}^-$.

The system under consideration does not have the symmetry of the full rotation group however. The symmetry is lowered by the crystal structure of the system. A zincblende bulk crystal has the symmetry of the pointgroup T_d . This point group has the same symmetries as a tetrahedron making it a subgroup of the full rotation group. The representations of the full rotation group induce representations in the subgroup T_d . These representations need not be irreducible and the decomposition of the restricted representations into irreducible representations of T_d is given by the branching laws (see Sec. 2.1), which can be found for example in the compatibility tables of reference [33].

For T_d as a subgroup of the full rotation group, the compatibility table gives that $D_{\frac{1}{2}}^+$ is restricted to Γ^6 . In other words, the first conduction band transforms according to Γ^6 . Light and heavy holes transform according to Γ^8 and the spin splitoff band transforms according to Γ^7 .

The theory of invariants now gives that there is a block in the Hamiltonian for each combination of two irreducible representations. This means that the Kane Hamiltonian can be written in 3×3 blocks.

$$\mathcal{H}_{8 \times 8} = \begin{pmatrix} H_{6c6c} & H_{6c8v} & H_{6c7v} \\ H_{8v6c} & H_{8v8v} & H_{8v7v} \\ H_{7v6c} & H_{7v8v} & H_{7v7v} \end{pmatrix} \quad (3.17)$$

It is also possible to take higher conduction bands transforming according to γ_{7c} and γ_{8c} into account. This would give a 14×14 dimensional Hamiltonian. Because the corrections induced by these bands is very small, these bands will not be taken into account explicitly. Note that in order to take Dresselhaus spin-orbit interaction into account, these bands cannot simply be ignored.

The theory of invariants (see Sec. 2.4) now tells us that each of these blocks can only be build up from invariants that belong to a representation that is in

the direct product of the two bands that it couples. This means that H_{6c6c} can only contain invariants contained in $\Gamma^6 \otimes \Gamma^6 = \Gamma^1 \oplus \Gamma^4$. The multiplication of two representations can be found with the help of the multiplication tables given in reference [33].

If all fields except for the momenta are set to 0 the Kane Hamiltonian is recovered up to some constant parameters. For the 6c6c block this means that

$$H_{6c6c} = E_c + c_{12}^{6c6c} k^2 \sigma_0, \quad (3.18)$$

for some constant c_{12}^{6c6c} . It makes sense to equate this constant with $\frac{\hbar^2}{2m_c}$ to identify this term with the kinetic energy of particles in the first conduction band. By proceeding similarly, the Kane Hamiltonian $H_{8 \times 8}$ can be recovered. For the explicit form of $H_{8 \times 8}$ see reference [29].

3.4 Application of Löwdin partitioning and theory of invariants

Using Löwdin partitioning, (see reference [29]), remote bands can effectively be taken into account instead of explicitly. Löwdin partitioning allows to determine an effective 2×2 Hamiltonian for the system. There are three invariants which are relevant for the bulk system. The constant energy proportional to σ_0 , the kinetic energy, proportional to $k^2 \sigma_0$ and the Rashba spin-orbit term proportional to

$$\vec{\sigma} \cdot \vec{k} \times \vec{E}. \quad (3.19)$$

Since energy is only defined up to an additive constant, the constant energy can be ignored. This means that the 2×2 Hamiltonian can be written as

$$H_{2 \times 2} = \frac{\hbar^2 k^2}{2m_c} \sigma_0 + r_{41}^{6c6c} \vec{\sigma} \cdot \vec{k} \times \vec{E}. \quad (3.20)$$

The value of m_c for bulk systems can be obtained from literature. A prediction for r_{41}^{6c6c} and nonbulk m_c can be obtained by Löwdin partitioning. The dispersion relation of this Hamiltonian is shown in Fig. 1.3a.

The dispersion relation can also be calculated from the full $H_{8 \times 8}$ Kane Hamiltonian. In order to do this however, the missing constants such as m'_c appearing in H_{6c6c} must be determined. In H_{8v8v} and H_{7v7v} , γ'_1 and γ'_2 appear to parametrize the effective masses in the Kane Hamiltonian. The other parameters are P , γ'_3 and the energy offsets E^{6c} , E^{7v} and E^{8v} . The unprimed parameters can be found in band structure parameter tables (e.g. ref. [29]). For the primed parameters only the unprimed versions can be looked up. The unprimed versions of the parameters correspond to the smaller effective models of the semiconductor. For m'_c , for example, one can only look up m_c appearing in Eq. (3.20) for the mass of the conduction band electrons where the other bands have been effectively taken into account. Calculating the primed parameters can be done by calculating m_c with a Löwdin partitioning of H_{6c6c} with unknown m'_c . This then gives a relation between m_c and m'_c which can be solved for m'_c .

There are two contributions to the invariant $\frac{\hbar^2 k^2}{2m_c}$. The first is from the H_{6c6c} block appearing as the first order in the Löwdin partitioning. The second is from the Γ^7 and Γ^8 valence bands in the full $H_{8 \times 8}$ Hamiltonian in the second

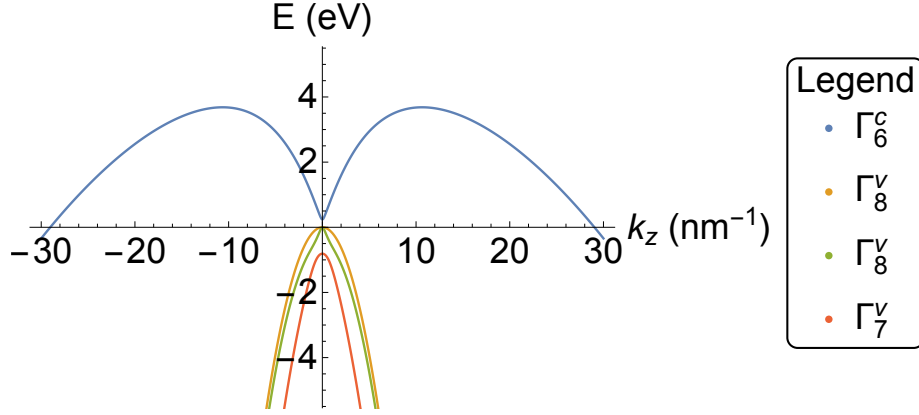


Figure 3.2: In this figure the dispersion relation of $H_{8 \times 8}$ is shown. From the figure it can be seen that the conduction band bends down for higher values of k .

order terms in the Löwdin partitioning. This leads to

$$\frac{\hbar^2}{2m_c} = \frac{\hbar^2}{2m'_c} + \frac{P^2}{3} \left(\frac{2}{E^{6c} - E^{8v}} + \frac{1}{E^{6c} - E^{7v}} \right), \quad (3.21)$$

or alternatively

$$m_c = \frac{1}{\frac{1}{m'_c} + \frac{2P^2}{3\hbar^2} \left(\frac{2}{E^{6c} - E^{8v}} + \frac{1}{E^{6c} - E^{7v}} \right)}. \quad (3.22)$$

The parameters γ'_1 , γ'_2 and γ'_3 can be calculated similarly. This defines all parameters of the $H_{8 \times 8}$ Hamiltonian.

Once these calculations are performed, it turns out that m'_c is negative. For small k , the conduction band is pushed up by the valence bands and the band bends up. For larger k however, the kinetic energy term starts to dominate and the conduction band bends down. This behavior is shown in Fig. 3.2.

In fig. 3.2 it can be seen that for some k_0 the conduction band crosses zero and it closes the gap of the system. It is important to note however that these solutions do not represent real solutions of the system. If one is not careful when determining the solutions of the system, the spurious zero energy solutions can drastically alter the result. For calculations in momentum space, all momenta must be much smaller than k_0 . For calculations in real space the situation becomes more complicated. The problem of the spurious solutions will be postponed until Chapter 4.

For bulk systems, it is now possible to calculate r_{41}^{6c6c} from this Hamiltonian. The electric field is treated as a small perturbation on the Hamiltonian appearing on the diagonal of the matrix. The Rashba term appears in the third order terms of the Löwdin partitioning. This expansions leads to

$$r_{41}^{6c6c} = \frac{eP^2}{3} \left(\frac{1}{(E^{6c} - E^{8v})^2} - \frac{1}{(E^{6c} - E^{7v})^2} \right). \quad (3.23)$$

This gives a first estimation of the strength of Rashba spin-orbit coupling. The system of interest, however, is not a bulk system. Considering nanowires instead

of bulk systems has two effects. Firstly the structure of the invariant changes and secondly, the confinement changes the Löwdin partitioning because the different subbands have to be taken into account. In the next section, these effects will be calculated.

3.5 A model for confined systems: Subband Löwdin partitioning

Changing from bulk systems to quantum well systems or nanowire systems breaks the symmetry of the system. These systems have respectively one and two confined directions that are no longer similar to the other directions. This means that the symmetry group is no longer T_d but a subgroup thereof. The orientation of the system relative to the tetrahedral symmetry group is important and gives rise to the growth direction which determines the relevant subgroup of T_d .

For this thesis, two growth directions of the nanowires are especially important. The [100] direction and the [111] direction. For nanowires the symmetry group of these wires can be determined by taking all elements of T_d that keep the orientation of the wire fixed. For the [100] direction, D_{2d} is obtained and for [111], C_{3v} is obtained. These groups give a different set of invariants that can arise in the system. Using the compatibility table to find which representation represents electrons, the representations for H_{6c6c} can be found. A representation of the unit cell of zincblende together with the growth direction is given in Fig. 3.3.

The invariants that can be used to expand the Hamiltonian depend on the symmetry group of the problem. Going to a subgroup reduces the symmetry of the system. Therefore the number of allowed invariants increases. The subgroups corresponding to either 2-dimensional quantum well systems or 1-dimensional nanowire systems have principle axis of rotation which is the \hat{z} -direction. This means that it is no longer necessary to treat every direction on the same footing. The bulk Rashba invariant (see Eq. (3.19)) splits in three new invariants. These are

$$E_z(k_y\sigma_x - k_x\sigma_y) \quad (3.24)$$

$$(E_yk_x - E_xk_y)\sigma_z \quad (3.25)$$

$$k_z(E_x\sigma_y - E_y\sigma_x). \quad (3.26)$$

For 2-dimensional quantum well systems, the relevant invariant has the wavevector in the \hat{x} - or \hat{y} -direction and the electric field along the \hat{z} -direction. Therefore the term in the Hamiltonian is

$$r_{41}^{6c6c} E_z(k_y\sigma_x - k_x\sigma_y). \quad (3.27)$$

For 1-dimensional nanowires, the only wavevector that can occur in the invariant is k_z . The electric field can then be applied in either the \hat{x} - or \hat{y} -direction. The term in the Hamiltonian takes the form

$$r_{41}^{6c6c} k_z(E_x\sigma_y - E_y\sigma_x). \quad (3.28)$$

For the [100] direction these invariants belong to the representation Γ^5 of the point group D_{2d} . One could therefore introduce new notations for coefficients of

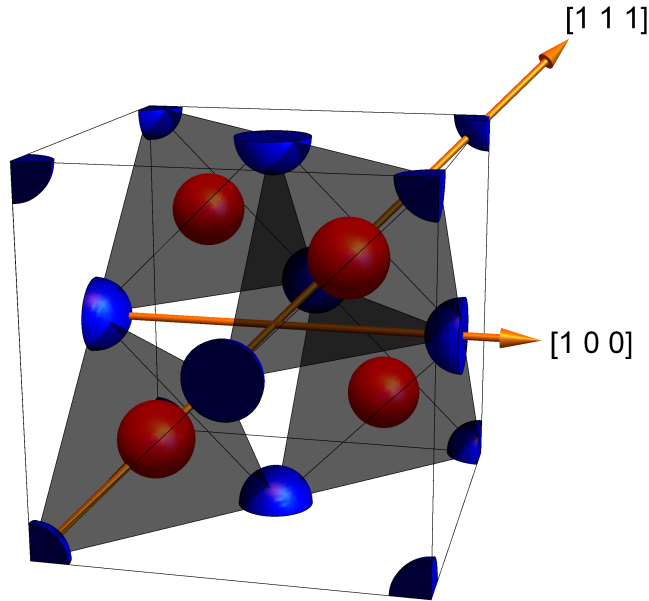


Figure 3.3: This figure shows the unit cell of a zincblende structure. The unit cell consists of two different types of materials, one shown in red and one in blue. The back shaded regions are four tetrahedrons and function as a guide to the eye. The $[100]$ and $[111]$ direction are shown with arrows.

the invariants. It will always be clear from the context however, which invariant is meant. Therefore, only the notation r_{41}^{6c6c} will be used in this thesis.

Besides the fact that the invariant has a different structure in systems with lower symmetry, the confinement itself also influences the wavefunctions in the system. This confinement results in discrete states. These subband states change the result of the Löwdin partitioning. In order to do this subband Löwdin partitioning, the 8×8 Kane Hamiltonian is expanded with respect to a set of basis states. Then Löwdin partitioning on this new matrix will be performed. This will then give an effective 2×2 matrix for one of the subbands of the conduction band.

To obtain a set of basis vectors, a new 8×8 Hamiltonian H_0 is defined. This H_0 is defined in such a way that it models all bands of the Kane Hamiltonian, but without coupling between the bands. Hence, H_0 can be written in block diagonal form as

$$(H_0)_{b_1, b_2} = \delta_{b_1 b_2} \left(-\frac{\hbar^2}{2m_{b_1}} (k_{\perp}^2) + V(\vec{r}) + E_{b_1} \right). \quad (3.29)$$

In this equation the vector \vec{k}_{\perp} denotes wavevector component perpendicular to all infinite directions in the system. The indices b_1 and b_2 take values in c, l, h, s for respectively the conduction band, light holes, heavy holes and the spin splitoff band. The eigenstates of this Hamiltonian can be calculated. There is an infinite number of subbands per band indexed by a quantum number i . Then the eigenstates can be denoted by $|\psi_{bi}\rangle$ and the following matrix can be

defined

$$H_{b_1 i, b_2 j} = \langle \psi_{b_1 i} | H_{8 \times 8} | \psi_{b_2 j} \rangle. \quad (3.30)$$

In order to apply Löwdin partitioning, the states described by this matrix have to be partitioned in two sets A and B . Let A consist of all states of the conduction band and B of all other states. Then, the hamiltonian must be split in three parts. The first part is a diagonal Hamiltonian, which is

$$H'_0 = \langle \psi_{b_1 i} | H_0 | \psi_{b_2 j} \rangle. \quad (3.31)$$

the second and third part, H_1 and H_2 respectively, contain the various coupling terms such that

$$H_{b_1 i, b_2 j} = H'_0 + H_1 + H_2, \quad (3.32)$$

where H_1 is a diagonal matrix.

The Löwdin expansion can be written in terms of the matrices $(H_1 + H_2)_{b_1, b_2}$. One has to take care however, that these terms are infinite dimensional matrices and do not commute with each other in general in contrast to the bulk case where the terms were just numbers.

The masses m_{b_1} in Eq. (3.29) must now be defined. For the conduction band the mass is known as this is a fundamental parameter of the material (c.f. [29]). For the spin splitoff band a similar calculation leads to $m_s = -m_0/\gamma_1$. In the case of 2-dimensional systems one can distinguish the heavy holes and the light holes which leads to $m_l = -m_0/(\gamma_1 + 2\gamma_2)$ and $m_h = -m_0/(\gamma_1 - 2\gamma_2)$ which are the parameters used in Chapter 4.

For 1-dimensional systems the directions are less clear and the difference between heavy holes and light holes is no longer clear. Therefore, the average of all masses appearing in H_{8v8v} is taken which leads to

$$m_l = m_h = \frac{-m_0}{6} \left(\frac{2}{\gamma^1 - \gamma^2} + \frac{2}{\gamma^1 + \gamma^2} + \frac{1}{\gamma^1 + 2\gamma^2} + \frac{1}{\gamma^1 - 2\gamma^2} \right). \quad (3.33)$$

The result in Chapter 5 are calculated using these values for m_l and m_h .

To keep the resulting formulas concise, the following notation is introduced

$$\Delta_{ij}^{b_1 b_2} = E_i^{b_1} - E_j^{b_2}. \quad (3.34)$$

In this notation b_1 and b_2 denote two bands and i, j denote two subband indices. The energies on the right hand side are the energies of the states $|\psi_{b_1 i}\rangle, |\psi_{b_2 j}\rangle$.

Performing the partitioning in practice taking these subband states into account is more involved than the bulk case. The theory of invariants can simplify the calculation though. The structure of the invariant is known from the beginning. If all terms that are not proportional to this invariant are removed from the calculation, a significant part of the terms can be removed from the calculation. If a term is not proportional to the electric field for example, it can never contribute to Rashba spin-orbit coupling. As the electric field enters the 8×8 Kane Hamiltonian only on the diagonal, it can be deduced that for third order Löwdin partitioning, the other terms on the diagonal do not enter the expansion.

Assuming that the wavefunction does not depend on the band b

$$|\psi_{bi}\rangle \equiv |\psi_i\rangle \quad (3.35)$$

and form an orthonormal basis

$$\langle \psi_{b_1 i} | \psi_{b_2 j} \rangle = \delta_{ij} \quad (3.36)$$

greatly simplifies the result of the calculation. This assumption ensures that the formula for m_c is independent on the explicit form of the wavefunctions. The result of the calculation for the conduction band mass is

$$\frac{\hbar^2 k^2}{2m_c} = \frac{\hbar^2 k^2}{2m'_c} + \frac{P^2}{6} \left(\frac{1}{\Delta_{ii}^{cl}} + \frac{3}{\Delta_{ii}^{ch}} + \frac{2}{\Delta_{ii}^{cs}} \right). \quad (3.37)$$

If the limit of this formula is taken to the bulk system, the subband indices can be suppressed and using $\Delta^{cl} = \Delta^{ch}$ the bulk equation for m_c can be recovered. Just as in the bulk case. The Rashba coefficient contains a term coming from the light hole band, and a term from the spin splitoff band. Similar to the bulk case, these terms are very similar but opposite in sign. Therefore the following notation is introduced:

$$T_{ij}^{cb} = (\langle \psi_{ci} | z | \psi_{bj} \rangle \langle \psi_{bj} | k_z | \psi_{ci} \rangle - \langle \psi_{ci} | k_z | \psi_{bj} \rangle \langle \psi_{bj} | z | \psi_{ci} \rangle) \times \left(\frac{1}{\Delta_{ii}^{cb} \Delta_{ij}^{cb}} + \underbrace{\frac{1}{2\Delta_{ii}^{cb} \Delta_{ji}^{cb}} - \frac{1}{2\Delta_{ij}^{cb} \Delta_{jj}^{cb}}}_{\tau} \right). \quad (3.38)$$

With this notation, the formula for the Rashba coefficient can be written as (see appendix D)

$$r_{41}^{6c6c} = \frac{-ieP^2}{3} \sum_j (T_{ij}^{cl} - T_{ij}^{cs}). \quad (3.39)$$

In the limit of a bulk system, the subbands lose their meaning which means that the i and j can be suppressed. The brackets reduce to $[k, k_z] = \iota$. In this limit Eq. (3.23) is recovered.

It is interesting to note that Eq. (3.39) does not fully agree⁷ with reference [29]. The terms denoted with τ in Eq. (3.38) are not present in the equivalent equation in reference [29] which can be written as

$$r_{41}^{6c6c} = \frac{-ieP^2}{3} \sum_j (T'_{ij}{}^{cl} - T'_{ij}{}^{cs}), \quad (3.40)$$

with

$$T'_{ij}{}^{cb} = (\langle \psi_{ci} | z | \psi_{bj} \rangle \langle \psi_{bj} | k_z | \psi_{ci} \rangle - \langle \psi_{ci} | k_z | \psi_{bj} \rangle \langle \psi_{bj} | z | \psi_{ci} \rangle) \times \left(\frac{1}{\Delta_{ii}^{cb} \Delta_{ij}^{cb}} \right). \quad (3.41)$$

In this thesis Eq. (3.39) will be used instead of Eq. (3.40). It is worth noting that the difference between the two equation is small. This can be seen from Fig. 4.2.

⁷The factor of -2 has been changed in the errata of reference [29].

3.6 Intermezzo: Bulk inversion asymmetry and Dresselhaus spin-orbit interaction

This section describes a different effect from Rashba spin-orbit interaction and can be skipped without breaking the continuity of the thesis. The unit cells of zincblende and wurtzite are not inversion symmetric. This means that the parity symmetry is broken and the reasoning of Sec. 3.2 does not a priori forbid spin-orbit interaction. The spin-orbit interaction that results from bulk inversion asymmetry (BIA) is called Dresselhaus spin-orbit splitting. In this section the appearance this effect will be investigated. It will be explained how one can derive symmetry conditions from the pointgroup of the system under investigation. In this section, only zincblende will be discussed but results for other structures can be derived similarly. Nanowires grown in the [111] direction will be given considerable attention for this is the most relevant system experimentally.

The pointgroup corresponding to the zincblende is T_d . All fermionic particles in the system must transform according to a representation such that a rotation of 2π changes the sign of the wavefunction (cf. Eq. (2.21)). These kind of representations are called double group representations [23]. The double group representations in T_d are Γ_6 , Γ_7 and Γ_8 , with dimensions 2, 2 and 4. Following the theory of invariants, the Hamiltonian must satisfy the symmetry induced by these representations. The representation corresponding to the first conduction band is Γ_6 , which is 2-dimensional. Therefore the Hamiltonian cannot assign different energies to the spin-up and spin-down particles. In other words, the two spin directions are degenerate. From the fact that all of the representations are higher dimensional it can be deduced that spin-orbit splitting is not allowed in the T_d symmetry group.

The situation changes when the symmetries of T_d are broken. Then the relevant symmetry groups become a subgroup of T_d and 1-dimensional *unirreps* can appear. There are 4 subgroups which are especially important and are denoted in table 3.1. From this table it can be deduced that the groups T_d , D_{2d} , and C_{2v} never allow for spin splitting. The group C_{3v} only allows for spin splitting in some bands and C_s always allows for spin splitting. Note however that if the symmetry group allows for spin splitting, this does not mean that the spin splitting must occur. So called accidental degeneracies can exist in the system [24].

The first effect of symmetry breaking that must be taken into account is the orbit of the spin-orbit coupling. By choosing a specific directions for the wavevector the symmetry of T_d is broken to a lower symmetry group. The resulting symmetry group depends on the direction of the wavevector. For k along the [100] direction, the resulting symmetry group is C_{2v} , for [111] the resulting group is C_{3v} and for [110] the resulting group is C_s . This means that the appearance of Dresselhaus spin-orbit interaction depends on the direction in the bulk system.

If non-bulk systems are considered the symmetry can be lowered even further. For a detailed description of all possibilities, cf. reference [34]. Most importantly for nanowires, the direction of the wavevector must always align with the growth direction of the nanowire. Therefore the results derived in the previous paragraph hold for nanowires as well. In a [111] nanowire, the conduction band electrons transform according to Γ_4 of C_{3v} . This means that no

Group	Double group representations
T_d	$\Gamma_6(2), \Gamma_7(2), \Gamma_8(4)$
D_{2d}	$\Gamma_6(2), \Gamma_7(2)$
C_{3v}	$\Gamma_4(2), \Gamma_5(1), \Gamma_6(1)$
C_{2v}	$\Gamma_5(2)$
C_s	$\Gamma_3(1), \Gamma_4(1)$

Table 3.1: In this table several pointgroups are given with their irreducible double group representations. The dimensionality of every representation is given in brackets. The information in this table is taken from reference [33]. Note that representations in different rows denote different representations, although their notation is the same.

spin-orbit is possible in [111] nanowires if no additional symmetry is broken.

This is often taken to mean that Dresselhaus spin-orbit interaction is not possible in [111] nanowires [34][35]. Rashba spin-orbit interaction is still possible in these systems because the electric field breaks an additional symmetry allowing for spin-orbit interaction. The same is true however for Dresselhaus spin-orbit interaction. If additional symmetries are broken, by strain, electric field or any other effect, there is no longer any reason to believe that Dresselhaus spin-orbit interaction cannot occur in these systems. There is always an electric field in the experimental devices for Majorana research, hence Dresselhaus could occur in these devices. Further research is needed to confirm this prediction and predict the strength of this effect.

4 Quantum well systems

4.1 Theoretical model for quantum well systems

In this chapter, focus will be shifted from general systems to 2-dimensional quantum well systems. The bulk system has three infinite spatial directions. A confinement potential in one direction will be added to the bulk system such that one direction becomes finite. In particular, the potential of an infinite square well is added to the problem such that a 2-dimensional quantum well system is obtained. The advantage of 2-dimensional quantum wells over 1-dimensional nanowires is that the quantum wells are computationally much more tractable and can be used to gain intuition for the problem. This chapter aims to provide a fundamental understanding and the full parameter space will not be explored. Hence, although the orientation of the underlying crystal in the well can be important, only quantum well systems in the [001] growth direction will be considered. Furthermore, only InSb quantum well systems will be investigated in this chapter.

First, in this section, a theoretical prediction will be obtained by using the results from Löwdin partitioning. In the remainder of this chapter, this theoretical prediction will be compared to numerical results. In order to obtain numerical results, a basis must be chosen. The bases considered here are the reciprocal space basis (see Sec. 4.2) and the real space basis (see Sec. 4.3). Both have different advantages and care must be taken not to introduce spurious solutions to the problem.

The confined direction in this chapter is the \hat{z} direction. This means that the \hat{x} and \hat{y} direction remain free infinite directions in the problem. Hence k_x and k_y remain good quantum numbers to label the states, while k_z is no longer a good quantum number. The confinement in the \hat{z} direction introduces discretized states. Hence the bulk problem changes to a subband problem. The subband index is denoted by i and the width of the quantum well by L .

The analytical results for the effective mass and the Rashba coefficient were already calculated. These results must now be applied to the 2-dimensional quantum well case. This means that the basis states in the system must be known such that the brackets in Eq. (3.37) and Eq. (3.39) can be calculated.

A very useful approximation is that the eigenstates of the system are the quantum well states such that every band is described by the wavefunction

$$\psi_n(z) = \sqrt{\frac{2}{L}} \sin\left(\frac{n\pi z}{L}\right), \quad (4.1)$$

where L denotes the width of the quantum well and n denotes the subband number. This means that the wavefunction is equal for all bands in the problem. The second advantage is that quantum well states form an orthonormal basis, and are known analytically. This means that the assumptions given by Eq. (3.35) and Eq. (3.36) in the derivation of Eq. (3.37) and Eq. (3.39) are satisfied.

With the width L the only undefined parameter, a theoretical prediction for the effective mass can now be made. The relation between the theoretical effective mass and the width of the quantum well can be made for the different subband indices. The result is shown in Fig. 4.1 where the value for the bulk prediction is given as well. More confined quantum well system (i.e. systems

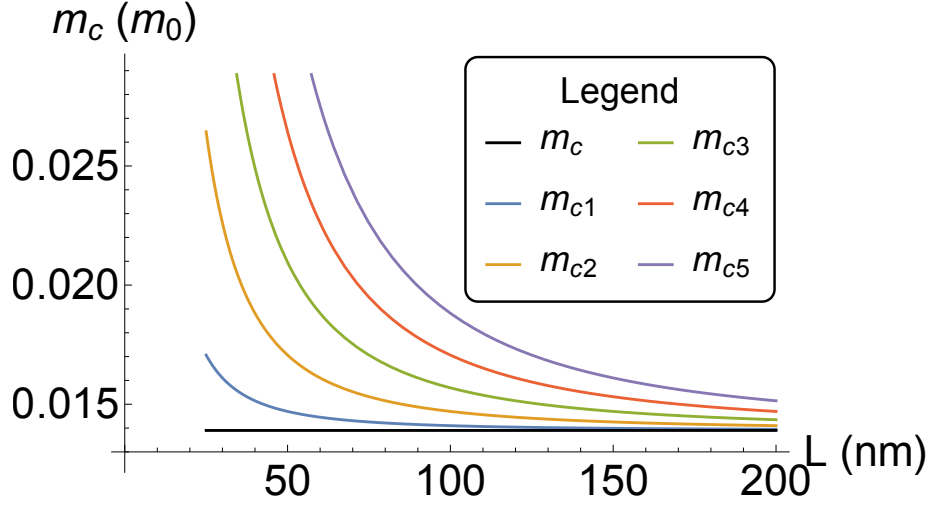


Figure 4.1: Theoretical prediction for the effective mass. This prediction is shown for the first five electron subbands. It can be seen that the value of the effective mass is predicted to increase as the width of the quantum well is decreased. Finally, the prediction for a bulk system is shown in black.

with a smaller width) exhibit larger effective masses for the conduction band than less confined systems.

For the theoretical prediction of the Rashba effect more work needs to be done. To evaluate Eq. (3.39) an infinite sum must be performed. In practice however, a cutoff can be introduced by neglecting the higher subbands that have a negligible contribution. The resulting equation still contains many terms, but this poses no computational difficulty. The width of the quantum well is the only unknown in the calculation and this relation between r_{41}^{6c6c} and L is shown in Fig. 4.2. Confined systems show a smaller Rashba spin-orbit strength than bulk systems and increasing the confinement leads to smaller values of r_{41}^{6c6c} .

The effect of the cutoff can be estimated by calculating the result for different values of the cutoff subband index. Both Eq. (3.39) and Eq. (3.40) are shown for comparison. The calculation converges very fast and for $n_{\max} \gtrsim 10$ the difference is no longer discernible. The value for the bulk calculation is given as a reference.

The theoretical predictions for the effective mass and the Rashba coefficient have now been obtained. These parameters together give the following Hamiltonian (cf. Eq. (3.20)):

$$H_{2 \times 2} = \frac{\hbar^2(k_x^2 + k_y^2)}{2m_c} \sigma_0 + r_{41}^{6c6c} E_z (k_y \sigma_x - k_x \sigma_y). \quad (4.2)$$

This means that for wave vectors in the \hat{x} -direction, the quantities k_{so} and E_{so} can be expressed in terms of r_{41}^{6c6c} (see Fig. 1.3a). Explicitly this gives

$$k_{\text{so}} = \frac{m_c r_{41}^{6c6c} E_z}{\hbar^2} \quad (4.3)$$

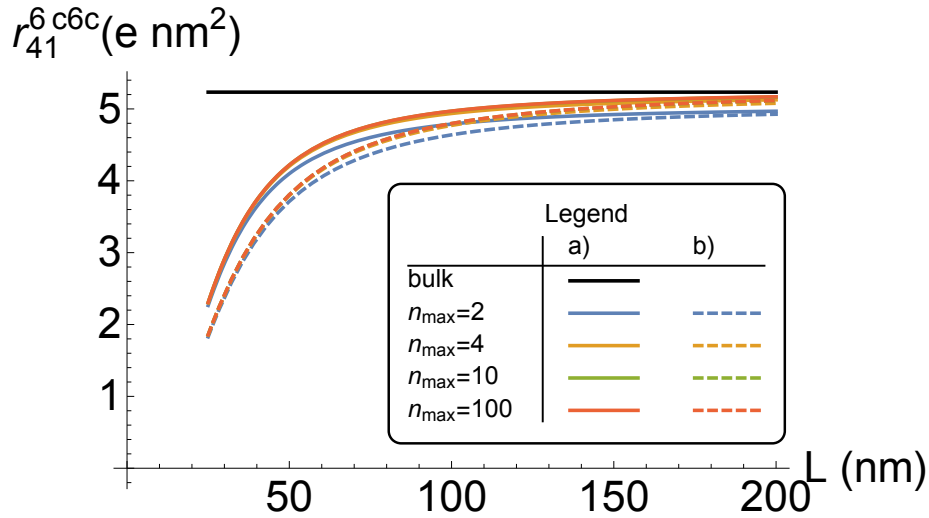


Figure 4.2: Theoretical prediction for r_{41}^{6c6c} for different values of the cutoff subband index n_{\max} . The solid lines correspond to Eq. (3.39) while the dashed lines correspond to Eq. (3.40).

and

$$E_{\text{so}} = \frac{m_c (r_{41}^{6c6c} E_z)^2}{2\hbar^2}. \quad (4.4)$$

The theoretical predictions of m_c and r_{41}^{6c6c} will be compared to numerical simulations in the remainder of this chapter. The value for m_c can be extracted from the curvature of band structure of the numerical simulation. The parameters k_{so} and E_{so} can be extracted from the lowest point in the band structure of the numerical simulations, see Fig. 1.3a. From these parameters the value of r_{41}^{6c6c} can be obtained via

$$r_{41}^{6c6c} = \frac{E_{\text{so}}}{k_{\text{so}}} \frac{2}{E_z}. \quad (4.5)$$

By choosing an appropriate basis to expand the Hamiltonian, it can be subsequently diagonalized to yield the band structure. These simulations will be the content of the rest of this chapter. First, the Hamiltonian is expanded in reciprocal space. Then the Hamiltonian is expanded in a real space basis.

4.2 Numerical simulations in reciprocal space

The finiteness in the \hat{z} direction of 2-dimensional quantum well systems introduces discretization in the system. In other words, k_z is no longer a good quantum number, but an operator acting on the subband state instead. The Hamiltonian of Eq. (3.17) contains the operators z and k_z which introduce coupling between the different basis states. The explicit form of this coupling must be investigated to perform the numerical simulations. In this section, momentum states will be used as basis states. The explicit form of these momentum states is

$$\psi_i(z) = \sqrt{\frac{2}{L}} \sin\left(\frac{i\pi z}{L}\right), \quad (4.6)$$

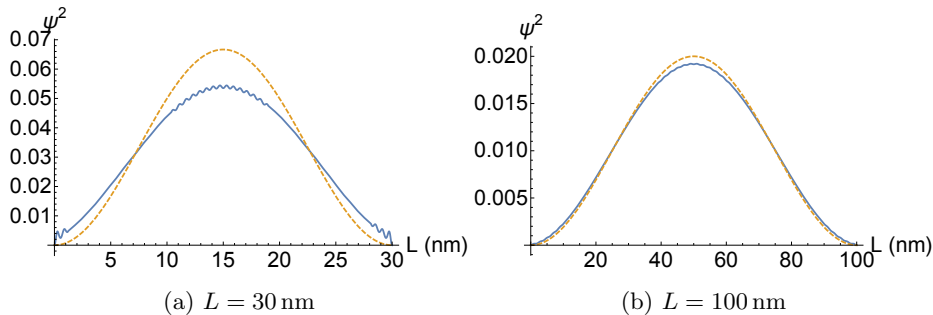


Figure 4.3: The spatial representation of the conduction electron wave functions. The left plot is for a quantum well width of 30 nm. The right plot shows the same plot for a width of 100 nm. The solid blue lines denote the result of the simulation. The dashed orange curves are the lowest quantum well states of Eq. (4.6).

where L denotes the width of the quantum well.

To take the subband structure into account the Hamiltonian must contain the coupling between the different basis states. The expanded Hamiltonian takes the form:

$$H_{b_1 i, b_2 j} = \langle \psi_i | (H_{8 \times 8})_{b_1, b_2} | \psi_j \rangle. \quad (4.7)$$

Linearity of the bracket means that the problem can be simplified. The operators k_x and k_y are good quantum numbers and therefore can be treated as numbers and taken outside of the bracket. Therefore many terms can be reduced to a form proportional to

$$\langle \psi_i | \psi_j \rangle = \delta_{ij}. \quad (4.8)$$

The remaining terms can be calculated analytically as well. For example, for $i \neq j$,

$$\langle \psi_i | k_z | \psi_j \rangle = \frac{2i(-1 + (-1)^{i+j})ij}{L(i^2 - j^2)}. \quad (4.9)$$

As can be seen in the denominator, coupling to remote basis states is small. In a similar way, the operators z and k_z^2 can be taken into account.

The expanded Hamiltonian can be diagonalized to find the eigenstates and eigenenergies of the system. In order to do a numerical diagonalization, the Hamiltonian must be finite. Therefore a cutoff momentum is introduced with the assumption that states with a higher momentum do not contribute to the problem. In the light of the spurious solutions this cutoff momentum must be lower than the point where the bands start to bend down. In doing so the spurious solutions are avoided and the eigenstates and eigenenergies can be calculated. The eigenstates for a quantum well of 30 nm and 100 nm are shown in Fig. 4.3. From this figure it can be seen that the approximation of quantum well states is justified for larger quantum well systems while for smaller quantum well systems a larger deviation from this approximation is observed. If the energy of the lowest energy conduction band is calculated for different values of k_x and k_y , a dispersion relation can be calculated. This dispersion relation can be compared to theory and the result is shown in Fig. 4.4a.

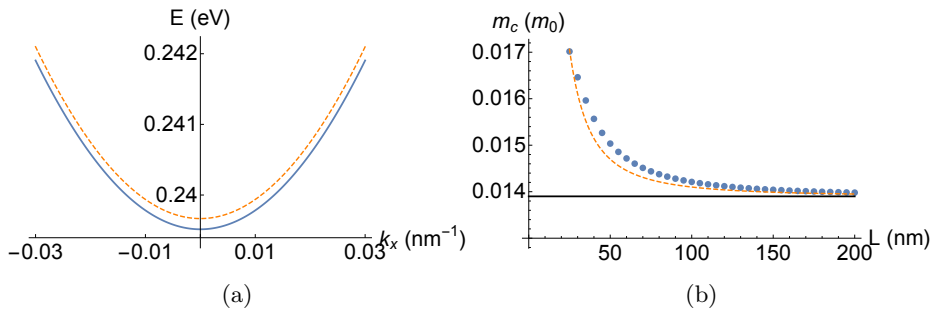


Figure 4.4: **Fig. a** shows the first conduction band. The solid curve denotes the result from the simulation. The dashed curve is the result of subband Löwdin partitioning with zero free parameters. The system under consideration is a 2-dimensional quantum well with $L = 100$ nm. **Fig. b** shows the simulated value for m_c as blue dots and the theoretical value of Eq. (3.37) by a dashed orange line.

By fitting the dispersion relation with a simple parabola the effective mass can be extracted. The model that is used for the fitting procedure is Eq. (3.20) where the field is fixed to zero. The result in Fig. 4.4b shows a very good qualitative agreement with the simulations. Adding confinement to the bulk system increases the mass. The physical picture to understand this result is that the conduction electrons are harder to squeeze through the system as the confinement is increased. The agreements between the analytical formula and the simulations also suggest that this simulation can be used as a baseline for the simulations in real space. This reciprocal space simulation can be compared with to conclude if the spurious solutions that arise in the real space simulations are dealt with without changing the system disproportionately.

4.3 Numerical simulations in real space

In the previous section, a momentum basis was chosen to construct the Hamiltonian. The upside of this method is that the spurious solutions are automatically avoided when introducing a momentum cutoff. The downside is that it is nontrivial to introduce spatial structures in the Hamiltonian. To perform simulations for nanowires, a basis must be chosen such that the confinement is taken into account. For a square or rectangular wire, one could use the quantum well states. For hexagonal wires, however, it is much harder to find suitable states to expand the Hamiltonian. Furthermore, it is hard to introduce more complicated and more realistic electric fields in the problem. For these reasons it is advantageous to investigate a real space basis for the problem.

This method discretizes space instead of momentum. For this 2-dimensional quantum well, a single line of lattice sites is needed to describe the subband states. Hence an evenly spaced chain of lattice sites will be considered with lattice spacing a . Wave functions will be described in this basis by their value on each of the lattice sites. The eigenstates of the position operator \hat{z} are then simply $\psi_i(z) = \delta_{z,ia}$ with eigenvalue z . The operator \hat{k}_z is more complicated in this basis.

Denote a state in this basis by a vector ψ containing a values on each lattice

sites. Then, a finite difference formula can be used to determine the derivatives

$$\frac{\partial}{\partial z}\psi(z) = \frac{\psi(z + \frac{1}{2}a) - \psi(z - \frac{1}{2}a)}{a}. \quad (4.10)$$

For higher derivatives of order n , Eq. (4.10) must be repeated n times. This gives the general form

$$\frac{\partial^n}{\partial z^n}\psi(z) = \frac{1}{a^n} \sum_{i=0}^n \binom{n}{i} (-1)^i \psi\left(x + \left(\frac{n}{2} - i\right)a\right). \quad (4.11)$$

For n odd, the lattice positions occurring in the formula are non-integer. To resolve this, the following approximation is made:

$$\frac{\partial^n}{\partial z^n}\psi(z) = \frac{1}{2} \left(\frac{\partial^n}{\partial z^n}\psi\left(z - \frac{a}{2}\right) + \frac{\partial^n}{\partial z^n}\psi\left(z + \frac{a}{2}\right) \right). \quad (4.12)$$

These equations yield the momentum operator in the real space basis, which is given explicitly by

$$k_z\psi(z) = -i\hbar \frac{\psi(z+a) - \psi(z-a)}{2a}. \quad (4.13)$$

With these equations, the brackets of Eq. (4.7) can be expanded and calculated. This procedure is very similar to the reciprocal space case of the previous section.

Calculating the eigenvalues of the expanded Hamiltonian yields a gapless system as shown Fig. 4.5a. Hence spurious solutions appear in the system. Before continuing they must be removed.

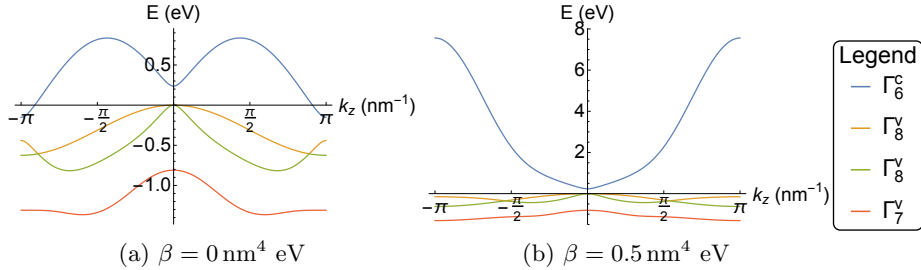


Figure 4.5: The dispersion relation is shown with and without k^4 -renormalization. Without the renormalization ($\beta = 0 \text{ nm}^4 \text{ eV}$) it can be observed that the gap is closed for higher values of k_z . With the renormalization ($\beta = 0.5 \text{ nm}^4 \text{ eV}$) the conduction band bends up for higher values of k_z .

In the reciprocal space, the spurious solutions could be avoided by introducing a momentum cutoff. In the real space representation, this is not possible. Hence a different solution must be used. The reason for the spurious solutions is the negative bare mass of the electrons. This causes the conduction band to bend down at high momentum. This effect is intensified by the discretization of space leading to a dispersion relation shown in Fig. 4.5a

To remove the spurious solutions the problem must be altered such that the bands no longer bend down at high momentum. One solution is called P

renormalization in which the parameter P is slightly altered together with the other parameters. This is done in such a way that at low k the systems closely resembles the original system, but the new system has a positive bare mass. As will be shown in the next chapter, this renormalization will not work for the purposes of this thesis and therefore a different solution will be employed.

Instead of altering the coupling parameters of the problem, a new term can be introduced in the Hamiltonian to counteract the spurious solutions while leaving the physical system the same. The simulations in this thesis all use the approximation that k is small, hence at those small k the Hamiltonian must remain as close as possible to the original. The term that will be used in this thesis is βk^4 . Here, β is a parameter to tune this extra term such that it is strong enough to make the conduction band bend up but not so strong that it will dominate the physical problem at small k . This solution is called k^4 -renormalization.

In the expanded Hamiltonian, the result of adding a k^4 term can be calculated from Eq. (4.11). This introduces coupling between lattice sites on z and $z \pm 2a$. This is called *next nearest neighbor hopping*. For the calculations in this section this introduces no problems. For the calculations in the next chapter, the unit cells are doubled by the next nearest neighbor hopping. This means that the Hamiltonian doubles in size making memory restrictions more stringent. To avoid confusion, k^4 is meant to mean $k_x^4 + k_y^4 + k_z^4$ for the purposes of k^4 -renormalization.

This renormalization is critical to the gap in the system. If the gap is closed by artificial discretization effects in the system, it is not to be expected that the results resemble either the theoretical predictions or experimental observations.

Now that the Hamiltonian is properly defined, it can again be diagonalized. The resulting band structure is shown in Fig. 4.5b. The figure shows that k^4 -renormalization is successful in preventing the conduction band bending down. Similar to the previous section, the lowest conduction band states are calculated for $L = 30$ nm and $L = 100$ nm. The result is shown in Fig. 4.6.

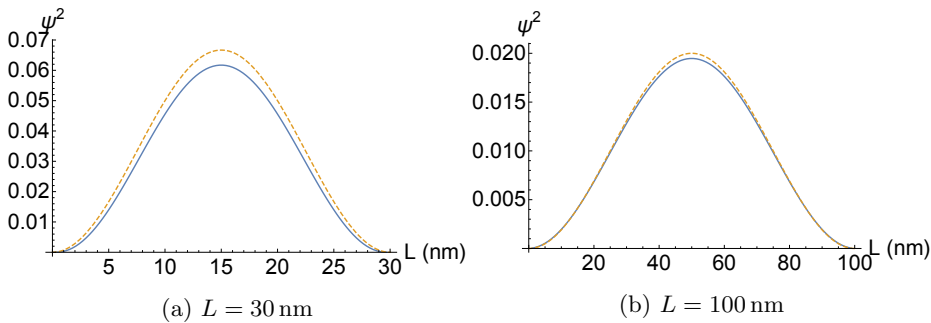


Figure 4.6: The eigenstates for the first conduction band are shown for a 2-dimensional quantum well. The left figure shows a quantum well of $L = 30$ nm and the right picture shows a quantum well for $L = 100$ nm. The solid blue lines denote the result of the simulation. The orange dashed line is the first theoretical quantum well state of Eq. (4.6). For these simulation k^4 -renormalization was used with $\beta = 1.0 \text{ nm}^4 \text{ eV}$

For the first three conduction bands, the effective mass can be simulated for

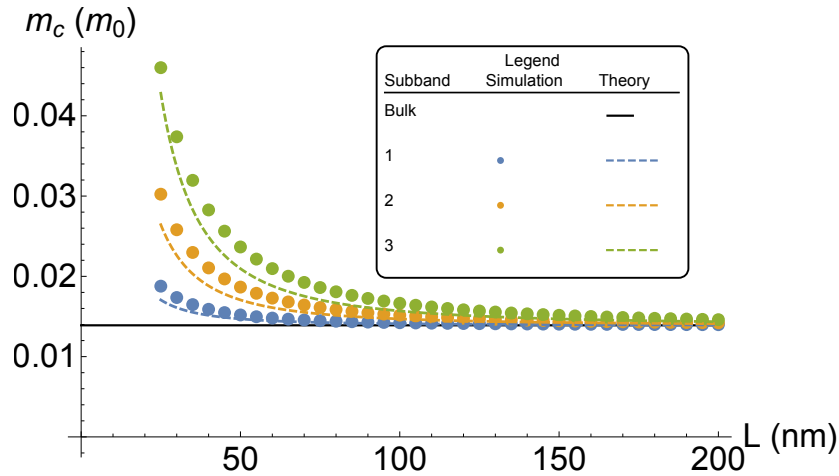


Figure 4.7: In this figure the effective mass is plotted for the first three conduction subbands. The result of the analytical formula is plotted with a dashed line. The points represent numerical simulations done for a 2-dimensional quantum well. Finally the bulk value of the effective mass is plotted with the black line.

different values of L (see Fig. 4.7). The result can be compared to the theoretical prediction and with the prediction for a bulk system. For larger values of L , the result indeed approaches the bulk value of the effective mass.

To show the effect of k^4 -renormalization, the energy of the first conduction band is plotted as a function of β . The result is shown in Fig. 4.8a. For large enough β , the band edges have been pushed to above the gap. The energy of the first conduction subband then becomes independent on β . Then r_{41}^{6c6c} is plotted as a function of β . In this plot, the electric field and the width of the quantum well are fixed. The width is $L = 100$ nm and $E_z = 0.0005$ eV nm $^{-1}$. In the plot it can be seen that the Rashba coefficient is very sensitive to β for the smaller values of β . If the band edges have been pushed to above the gap, the value of r_{41}^{6c6c} becomes less sensitive to β . The Rashba coefficient then converges to the theoretical bulk value for higher values of β .

Finally the Rashba coefficient can be calculated for a fixed value of $\beta = 1$ nm 4 eV and the electric field $E_z = 0.0005$ eV nm $^{-1}$. The value of r_{41}^{6c6c} is calculated from the simulations by using Eq. (4.5) for the first three conduction subbands. The result of the analytical formula (see Eq. (3.39)) is shown as well together with the bulk value for the Rashba coefficient. The result is shown in Fig. 4.9.

In the figure it can be seen that for large values of L the simulations reflect the bulk properties. For smaller values of L , the difference between the simulations and the theoretical predictions become appreciable. Especially for the higher subbands the difference is significant. In practice however, the lowest conduction band is the most interesting one and the width of the systems under consideration is $L = 100$ nm for the Majorana nanowire systems.

The results from the previous section show similar behavior as the results of this section. In particular, the approximations made by the theoretical model in Sec. 4.1 break down when the width of the quantum well drops below $L \approx 30$ nm.

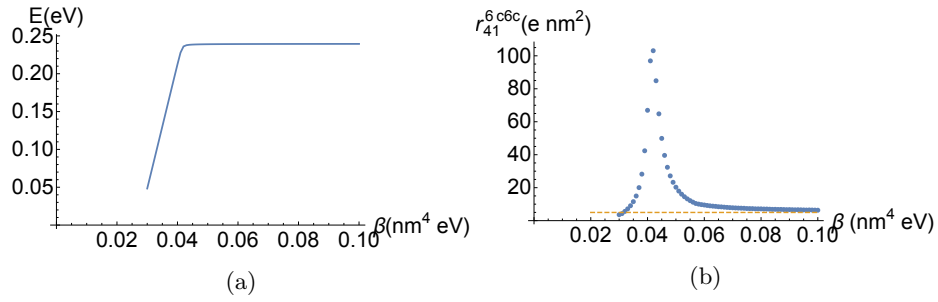


Figure 4.8: **Fig. a** shows the energy of the lowest conduction band for varying value of β . From this figure it can be seen that if the bands are pushed up far enough, the energy of the lowest conduction band no longer changes and represents the energy of the state with $k = 0$. **Fig. b** Shows the Rashba spin orbit strength r_{41}^{6c6c} for a varying value of β . The orange dashed line represents the theoretical value.

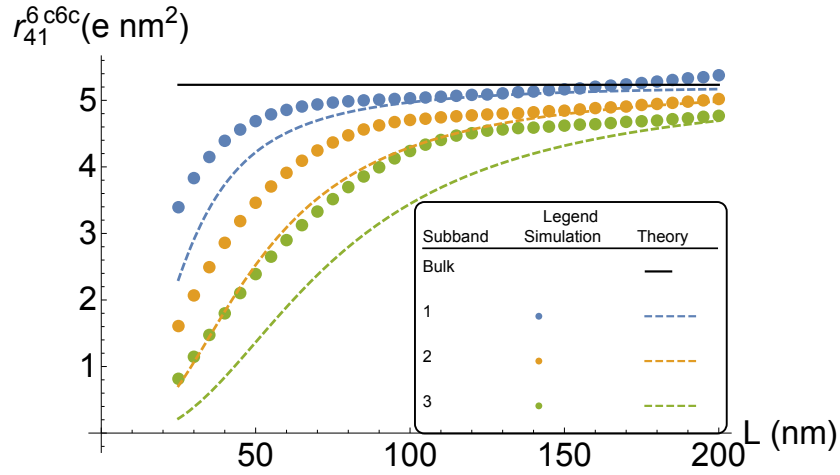


Figure 4.9: In this figure the dependence of r_{41}^{6c6c} on L is shown. The simulated values are shown with dots for the first three conduction subbands. The result for the theoretical prediction is shown with a dashed line. The black line denotes the bulk prediction for the Rashba coefficient.

In the next chapter, these 1-dimensional nanowire systems will be investigated in much the same way as this section. From the next chapter, more definitive answer can be obtained on the effective difference between theory and simulation for the relevant systems.

5 Nanowire systems

5.1 Theoretical model for nanowire systems

The 2-dimensional quantum well, as considered in the previous chapter, is obtained from the bulk system by adding confinement in one spatial dimension. To obtain a wire from the bulk system, the confinement is added to two spatial dimensions, which in this thesis are chosen as the x and y directions such that the z direction is the only free, infinite direction left in the system. The confinement potential is zero inside the region of the wire and infinite outside this region.

To obtain a theoretical prediction from the Löwdin partitioning for the 1-dimensional wire, basis states commensurate with the wire must be constructed. Similar to the quantum well case, particle in a (2-dimensional) box states will be used, forming a square nanowire with width L . This means that the states can be denoted with quantum numbers k_z , i and j .

With these states, Eq. (3.37) and Eq. (3.39) can be evaluated. For the 1-dimensional problem, not only the lowest subband will be considered, but also higher subbands. The theoretical predictions can be obtained separately for all different subbands as a function of L . For the effective mass, the obtained prediction is shown in Fig. 5.1. The two quantum numbers i and j are exchangeable without a electric field present. This explains that some subband states have identical effective masses.

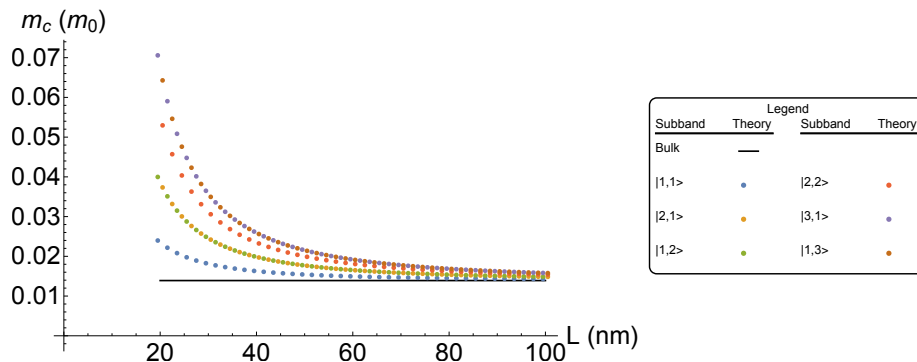


Figure 5.1: This figure shows the prediction for the effective mass for the six lowest conduction band states versus the width L of the nanowire. The result for a bulk system is shown in black.

For the Rashba coefficient r_{41}^{6c6c} , a corresponding prediction can be obtained. In Fig. 5.2 the result is shown. It is interesting to note that the presence of the electric field breaks the symmetry between the quantum numbers i and j . This is reflected by a small difference in the prediction for the $|2, 1\rangle$ and $|1, 2\rangle$ subband state. Similar to the quantum well case, confinement leads to smaller spin-orbit interaction.

In the remainder of this chapter the influence of the parameters of the system is studied. The parameters under consideration are the shape, growth direction and the material. Simulations will be used to investigate these parameters. The next section will describe the method used for these simulations. From

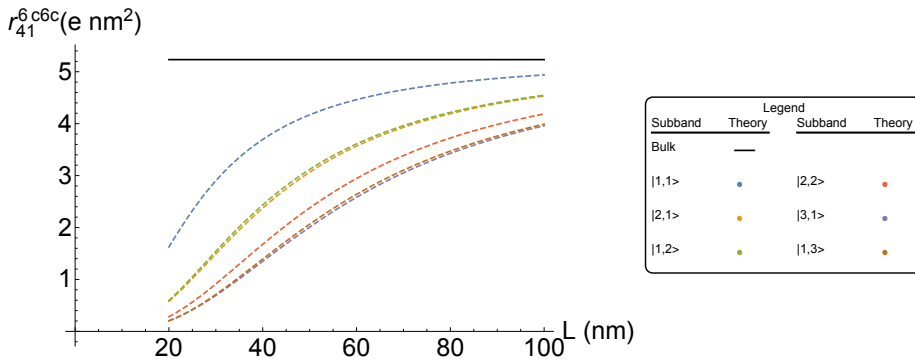


Figure 5.2: This figure shows the relation of r_{41}^{6c6c} (cf. Eq. (3.39)) and the width L of the wire. The result is shown for the six lowest conduction band states with dashed lines. The result for a bulk system is shown with a black line.

the simulations it is possible to obtain k_{so} and E_{so} (cf. Fig. 1.3a). This can be converted to a value for r_{41}^{6c6c} by Eq. (4.5) which can be compared to the theory of this section. In Sec. 5.3 a range of simulations is discussed where the electric field is modeled by a constant value over the wire area. In Sec. 5.4 the constant electric field is replaced by a more realistic electric field for the Majorana devices.

5.2 Method for numerical simulations of 1-dimensional systems

The nanowire simulations of this chapter are computationally much more challenging than the 2-dimensional quantum well simulations because the number of quantum numbers of a state has increased dramatically. Therefore this section is devoted to explain the method for performing these numerical simulations.

In the 2-dimensional case, states could be described by the quantum numbers k_x, k_y and the functional form on the 1-dimensional lattice. This means that for a lattice of 100 points, there is a 800×800 matrix that must be diagonalized. The factor of 8 comes from the fact that there are 8 different bands in the Hamiltonian (see Eq. (3.17)). For a 1-dimensional quantum wire, the functional form of the eigenstates must be determined on a 2-dimensional lattice. This means that if the wire is built on a 100×100 lattice, the matrix that is to be diagonalized is $80\,000 \times 80\,000$ dimensional. This takes considerably more time so one has to be careful when defining the parameters of the simulation.

It is also more difficult to write down the matrix because each lattice site now couples in four directions instead of two. When k^4 -renormalization is used, each site couples to 8 other sites which further complicates the construction of the Hamiltonian. The software package *Kwant*[36] is used to make this problem more tractable. Instead of specifying the matrix explicitly, in *Kwant* one can define the lattice sites in the system. Then one can define the onsite and hopping energies of each site, while *Kwant* keeps track where the hoppings lead to. Then *Kwant* constructs a sparse matrix of the problem which can then be subsequently diagonalized.

The quantity of interest in this chapter is E_{so} and k_{so} or equivalently r_{41}^{6c6c} .

This means that the minima of the bands need to be found. For each wavevector, the matrix must be diagonalized, which takes considerable time. In the previous section, the simulation times were sufficiently short to be able to sample the entire band and subsequently selecting the minimal point but for the simulations in this chapter this method is no longer feasible. Therefore a method is employed to minimize the number of diagonalizations. The shape of the band is always roughly the same in that it contains a single minimum at $(k_{\text{so}}, E_{ij} - E_{\text{so}})$ where E_{ij} denotes the energy of the subband state $|i, j\rangle$ at $k = 0$. This similarity in shape can be used to decrease the number of steps needed to find k_{so} .

The method used in this thesis is based on the golden section search algorithm [37]. The implementation can best be described recursively. Start with three points k_1 , k_3 and k_5 corresponding to the search window for k_{so} and diagonalize the matrix for these points. Then diagonalize the matrix for $k_2 = \frac{k_1+k_3}{2}$ and $k_4 = \frac{k_3+k_5}{2}$. Then select the point k_i for which the result is minimal and repeat this process with the three points k_{i-1} , k_i and k_{i+1} . Each iteration gives a better estimation of the minimal point. One can terminate this process once the accuracy goal has been reached. The algorithm can be optimized by noting that not both the point at k_2 and k_4 can be smaller than the point at k_3 . By making better choices for the location of $k_1 \dots k_5$ the algorithm can be optimized further.

Another problem occurs when the matrix is diagonalized. A numerical process is used that gives n eigenvalues of the matrix around a certain point in energy denoted by σ . Selecting the first several conduction bands is then a non-trivial task because the value of the gap changes depending on the electric field. Therefore it is hard to estimate a priori what σ should be. It is however possible to know whether σ is too high or too low. When σ is too high, no valence band states are found (i.e. no solutions with $E < 0$ are found). If σ is too low, no solutions are found with $E > 0$. With this information σ can be adjusted at runtime, to retry finding the first few conduction bands. The fastest algorithm in general would be a binary search algorithm. It is however possible to give a reasonable estimation of σ as initial value. Then the proper value of σ can be found by increasing or decreasing this parameter by a small amount. The value of σ does not require a high accuracy such that this method terminates within a few iterations.

5.3 Numerical simulations in constant electric fields

The field used to break the spatial inversion symmetry in this section will be a constant electric field. This leads to a linear potential of the form

$$V(x) = E_x x. \quad (5.1)$$

This form can be implemented on the lattice sites of the simulations. Although this form of the electric field is not represented by physical systems, the simulations in this section can be used to gain intuition for various parameters. First the subband behavior and lattice spacing parameter are studied. Then the dependence on growth direction, shape and material are studied.

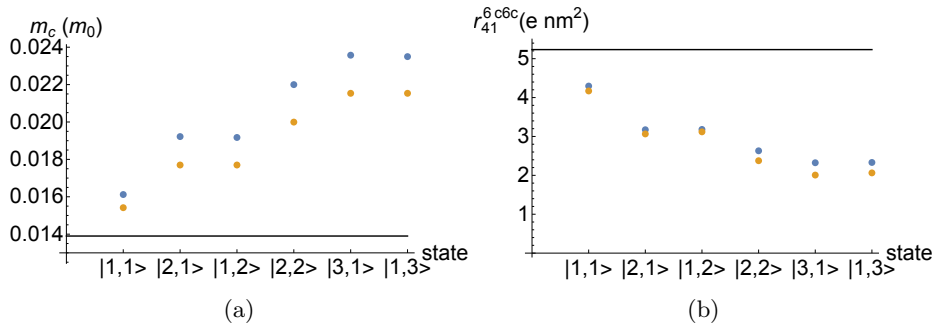


Figure 5.3: These figures are the result of simulations with parameters $E_z = 180 \mu\text{eV nm}^{-1}$, $L = 50 \text{ nm}$ and $\beta = 1 \text{ nm}^4 \text{ eV}$. The results from the numerical simulation are shown in blue. The results from the theoretical model for the bulk system are shown in black, the results from the theoretical model for a square nanowire are shown in orange. The horizontal axes denote the different subband states. **Fig. a** shows the value for m_c for the first six conduction band states calculated with Eq. (5.2). **Fig. b** is similar to **Fig. a** but shows r_{41}^{6c6c} .

5.3.1 Dependence on subband number

Similar to the previous chapter, the simulations can be used to investigate multiple subbands. In this subsection the effective mass and the Rashba coefficient will be investigated for the first six subbands. The simulations give the value for k_{so} and E_{so} from which r_{41}^{6c6c} can be calculated with Eq. (4.5). The effective mass m_c can be calculated with

$$m_c = \frac{\hbar^2 k_{\text{so}}^2}{2E_{\text{so}}}. \quad (5.2)$$

The result of the theory and the simulation for the effective mass is shown in Fig. 5.3a. The corresponding result for the Rashba coefficient is shown in Fig. 5.3b.

From these figures it can be seen that the theory shows reasonable agreement with the simulations. Especially the lowest conduction subbands shows good agreement with the theory which is the most important subband in this thesis. For this reason the rest of the parameter space will only be explored for this lowest subband state. The lattice spacing, the growth direction and the shape of the nanowire will be investigated in the next subsections.

5.3.2 Dependence on lattice spacing

In the previous chapter, it has not been investigated how the number of lattice sites influences the result. If the width of the nanowire is fixed, increasing the number of lattice sites means decreasing the distance between two lattice sites. This distance is denoted with a . All quantum well simulations of the previous chapter were performed with 100 lattice sites on a 1-dimensional chain. For a two dimensional lattice that is considered here, the number of lattice sites N is proportional to a^{-2} . This means that increasing a means decreasing computational time significantly. Besides different numbers of lattice sites, different values for β were chosen as well. The bulk value for r_{41}^{6c6c} is shown together with

the theoretical value for a nanowire system. The system under consideration was a nanowire with width $L = 50$ nm.

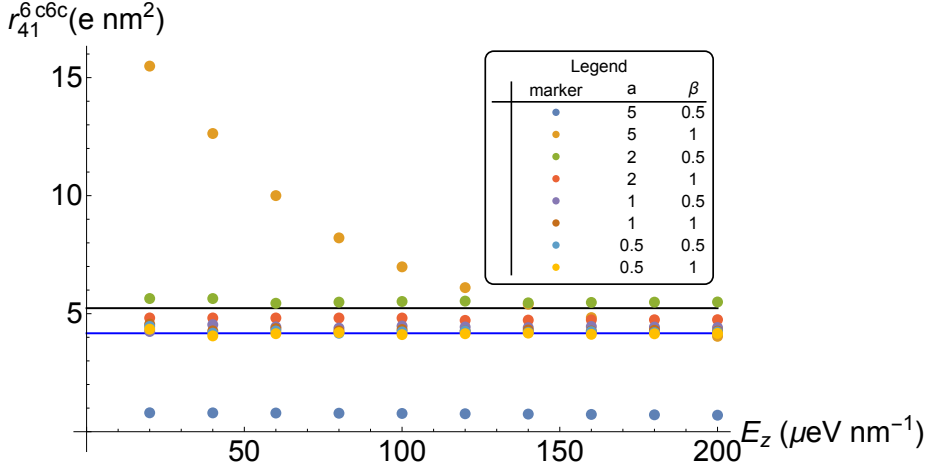


Figure 5.4: This figure shows the value of the spin orbit strength r_{41}^{6c6c} as it depends on the electric field E_z . For different values of lattice constant a , the simulations were performed. The system under consideration has width $L = 50$ nm. For each value of a the simulations were done for both $\beta = 0.5 \text{ nm}^4 \text{ eV}$ and $\beta = 1 \text{ nm}^4 \text{ eV}$. The black line shows the bulk value for r_{41}^{6c6c} given by Eq. (3.23). The theoretical prediction for a confined nanowire is shown in blue.

From Fig. 5.4 it can be observed that for lattice spacings of $a = 5$ nm the results are very far from the theoretical predictions. Furthermore the difference between $\beta = 0.5 \text{ nm}^4 \text{ eV}$ and $\beta = 1 \text{ nm}^4 \text{ eV}$ is enormous. If the lattice constant is decreased to $a = 2$ nm, the results are already more well behaved. By decreasing the lattice constant even further, the results come closer to the theoretical prediction. In order to keep simulation times manageable the remaining simulations in this chapter will be performed with $a = 1$ nm.

Theory predicts that r_{41}^{6c6c} does not depend on the value of the electric field. This property is violated by the $a = 5$ nm simulations. It is reflected by the other simulations, although only a small variation can be seen in those simulations. This variation from a straight line is more apparent in the next section, in Fig. 5.5.

5.3.3 Dependence on growth direction

Another aspect which has been ignored up until now is the growth direction of the crystal, but in this section the effects of the growth direction will be investigated. The growth direction of the nanowire denotes the infinite direction in the nanowire relative to the crystal of the underlying material. Two directions are especially important in this thesis. The $[100]$ direction is computationally very convenient and has therefore been used for all simulations up until now. The nanowires used for the Majorana experiments are nanowires grown in the $[111]$ direction. Although this direction is experimentally more relevant, it is computationally more difficult. These two growth directions are shown relative to the crystal structure in Fig. 3.3.

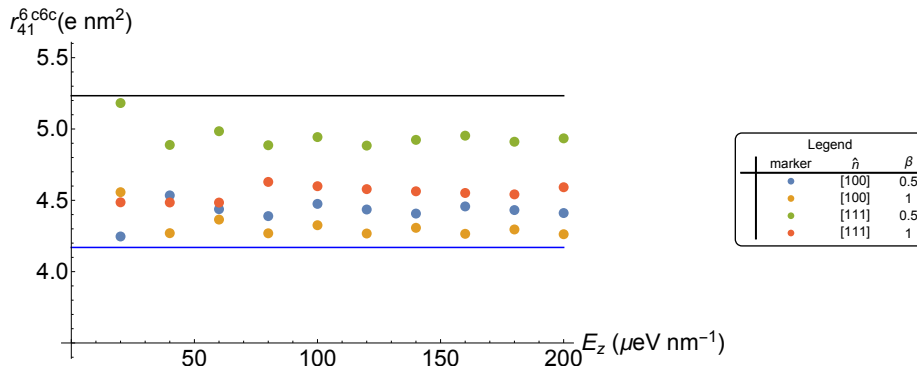


Figure 5.5: This figure shows two different nanowire systems with width $L = 50$ nm. The two systems have respectively growth directions [100] and [111]. For various values of the electric field and β the value of the Rashba coefficient r_{41}^{6c6c} is given. In black, the bulk value for r_{41}^{6c6c} is shown. In blue the result of the subband Löwdin partitioning is shown.

The spin orbit strength is calculated for two different values of β and the two different growth directions, [100] and [111]. Various values for the electric field are used. All results are relatively close together. This means that the variation for the different values of the electric field can be seen more clearly than in Fig. 5.4. The result for a nanowire of width $L = 50$ nm is shown in Fig. 5.5.

In the figure it can be seen that there is no significant difference between the two growth directions. The values for the [100] direction are a bit closer to the theoretical prediction. The spin orbit interaction is a bit larger in the [111] direction. The difference between the two growth directions is 5% for this system. As other differences in the thesis are larger, this effect will not be explicitly taken into account. The increased computational difficulty of the [111] direction prevents extensive research of this effect. In Sec. 5.4.2 another result for the [111] is calculated and in this case, the result is negligible further justifying the choice to neglect the growth direction.

5.3.4 Comparison between nanowire shapes

For 2-dimensional quantum well systems, only one shape of the system exists. This is the 1-dimensional chain. For 2-dimensional lattices however, more shapes can be chosen. All results shown in the previous section were for square nanowires. Square and hexagonal wires are equally difficult to simulate, but the theoretical prediction is much harder for hexagonal wires. For square wires all brackets and energies occurring in Eq. (3.39) can be calculated. This is because the eigenstates for a square system with an infinite confining potential are very similar to the normal quantum well states. For hexagonal systems, these eigenstates are not so simple. In this section, it will be investigated if the theory for hexagonal wires must be derived separately, or that the theory for square wires can be used for the hexagonal wires as well.

The width of a hexagonal nanowire is no longer defined uniquely. In this thesis, the width of a nanowire will be defined according to Fig. 5.6. From this

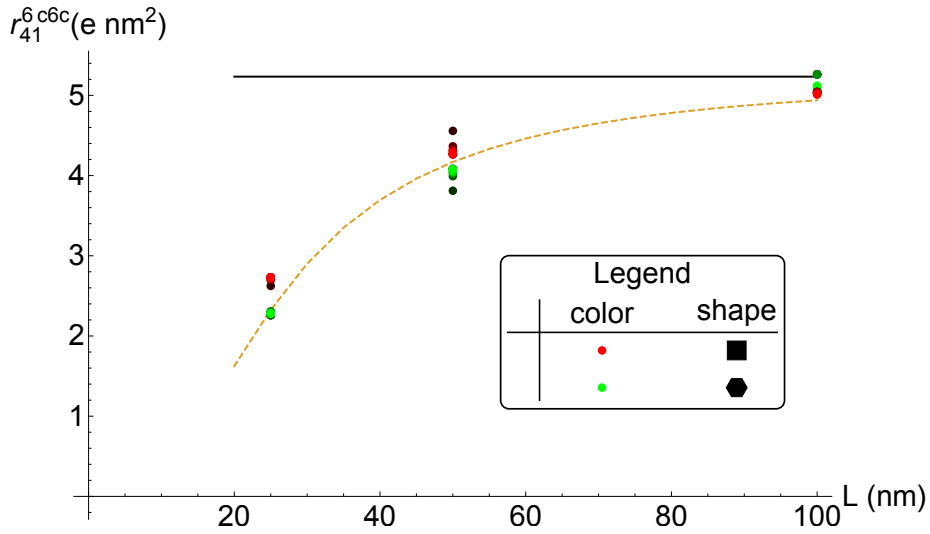


Figure 5.7: This figure shows r_{41}^{6c6c} as a function of the width L . Both square and hexagonal wires are used for the simulation. The parameter $\beta = 1 \text{ nm}^4 \text{ eV}$ is used. The different values are representing by showing points corresponding to a smaller field by darker points. The field ranged from $E_z = 10 \mu\text{eV nm}^{-1}$ to $E_z = 100 \mu\text{eV nm}^{-1}$. The black line shows the bulk value for r_{41}^{6c6c} while the orange dashed line corresponds the the subband value given by Eq. (3.39).

figure it can be seen that the area of a hexagonal nanowire is smaller than the area of a square nanowire with the same width L for this choice of the definition of L .

For nanowires of different widths and shapes the Rashba coefficient is calculated. The result is shown in Fig. 5.7. different values for electric field were simulated. Points corresponding to a smaller electric field are shown with a darker color.

From the figure it can be seen that the two different shapes yield different results, but for nanowires of $L = 100 \text{ nm}$ the difference can be neglected. The width of the hexagonal nanowires used in the Majorana experiment is large enough to neglect the difference in shape. Therefore no separate theory will be developed for hexagonal wires. In the next section (i.e. Sec. 5.4) hexagonal wires are used to calculate the electrostatic environment, so then the numerical simulations must use hexagonal wires as well to keep the shape of the field compatible with the simulation.

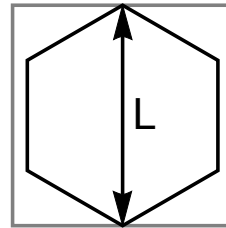


Figure 5.6: This figure shows a cross section of a square nanowire in gray and a hexagonal nanowire in back. They are both defined by the same width L .

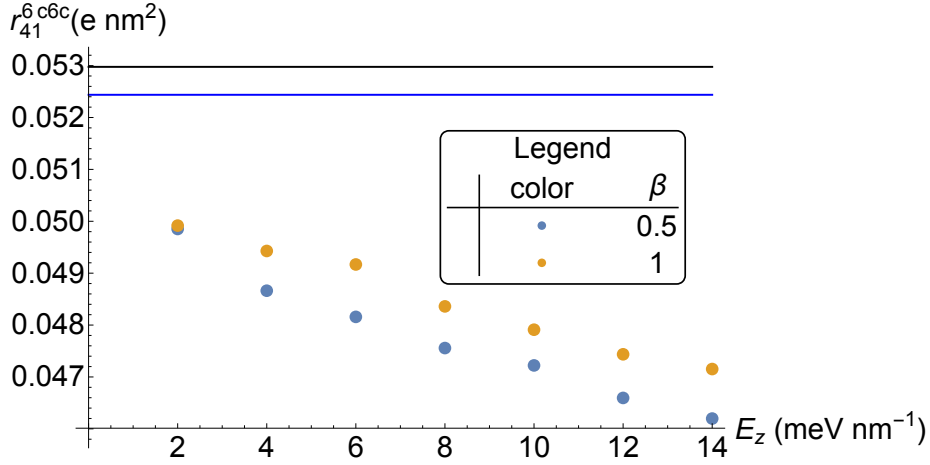


Figure 5.8: The system under consideration is a square GaAs nanowire of width $L = 50$ nm with growth direction $[100]$. The magnitude of the spin orbit interaction is shown for different values of the electric field. The different colors indicate $\beta = 0.5$ nm⁴ eV and $\beta = 1$ nm⁴ eV. The black and blue lines correspond to the bulk and subband theory respectively.

5.3.5 Dependence on Material of the nanowire

For the Majorana device, InSb nanowires are used. This makes InSb the most interesting material for the simulations as well. To test the generality of the simulations and the theory, this section will investigate a different material, GaAs in particular. For InSb the bulk value for the Rashba spin orbit interaction was shown a few times already. It can be calculated with Eq. (3.23) and the result for InSb is

$$r_{41}^{6c6c} = 5.23 \text{ e nm}^2. \quad (5.3)$$

This result only depends on the material under consideration. Therefore all results in this thesis show correspondence to this value. The actual value depends on the system geometry as was shown before. Changing the material has a large influence on the Rashba coefficient. The bulk value in GaAs systems is given by:

$$r_{41}^{6c6c} = 0.0530 \text{ e nm}^2. \quad (5.4)$$

Hence the Rashba spin orbit splitting in GaAs is expected to be 100 times weaker than in InSb systems, for similar electric fields. The magnitude of r_{41}^{6c6c} depends strongly on Δ_0 as can be seen from Eq. (3.19).

In agreement with this prediction, the results of the numerical simulations indeed show a much weaker spin-orbit interaction, as is shown in Fig: 5.8. In order to obtain a appreciable E_{so} larger values for the electric fields are used to simulate the nanowires in order to compensate for the weaker spin-orbit interaction. Again, different values for β are used to indicate that this parameter has a non-negligible influence on the resulting value for r_{41}^{6c6c} .

5.4 Numerical simulations in simulated electric fields

In contrast to Sec. 5.3 where a constant electric field is used to break the structure inversion symmetry, this section describes the results when this symmetry is broken by an electric field that follows from electrostatic simulations. The electric fields are obtained by solving the Schrödinger equation and the Poisson equation self consistently which is done by a Schrödinger-Poisson solver implemented by Adriaan Vuik as described in reference [22]. The Poisson equation is solved in the geometry of the real Majorana devices and the Schrödinger equation is solved for the 2×2 Hamiltonian from Eq. (3.20) with $r_{41}^{6c6c} = 0$. The resulting potential as a function of position given by

$$V : \mathbb{R}^2 \rightarrow \mathbb{R} : (x, y) \mapsto V(x, y). \quad (5.5)$$

An image of the geometry is shown in Fig. 5.9 in which the important parameters for the electrostatic simulation are given. The geometry of the system is described by the width L of the nanowire and the superconducting coverage of the nanowire given by c_0 . The parameter V_g denotes the voltage of the gate underneath the dielectric and V_{sc} denotes the effective voltage of the superconductor arising from a potential work function difference. For two different instances of these voltages the resulting energy potential

$$E_{\text{pot}}(x, y) = -eV(x, y) \quad (5.6)$$

are shown in Fig. 5.10.

The simulations considered in this thesis diagonalize the Hamiltonian to construct the band structure of the system for which it is enough to obtain the eigenvalues of the Hamiltonian matrix. The numerical diagonalization calculates the eigenstates as well however and these can be used to show the wavefunction of the lowest conduction band. For the energy potential given in Fig. 5.10a the conduction band is calculated with both p-renormalization and k^4 -renormalization and shown in Fig. 5.11. The resulting wavefunctions differ a lot. For the p-renormalization case, the wavefunction oscillates strongly close to the edges of the nanowire. Physical intuition suggests that the state should resemble the particle in a box ground-state. This is the behavior shown by the k^4 -renormalization case. Therefore all simulations in this thesis were performed using k^4 -renormalization rather than p-renormalization.

For $V_{sc} = 0.2 \text{ V}$, $V_g = -0.2$ the resulting energy potential is also calculated and shown in Fig. 5.10b. The interplay between the gate voltage and the super-

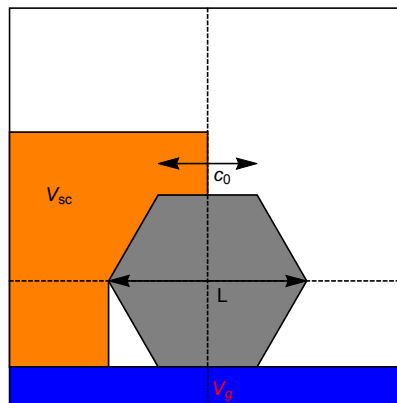
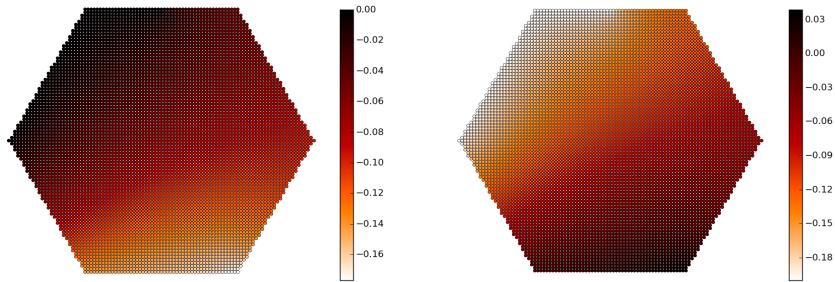


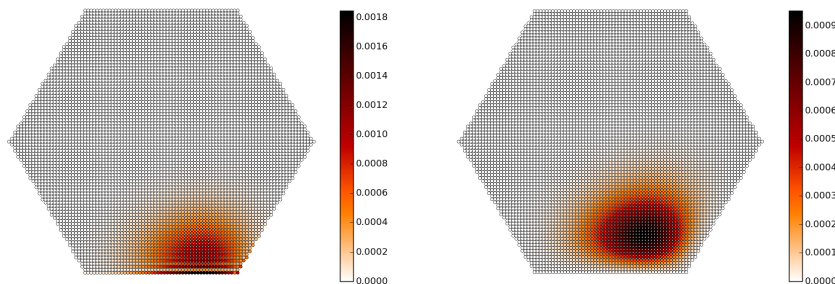
Figure 5.9: The geometry of the Majorana device. The wire is shown in gray, the superconductor in orange and the dielectric in blue. The width of the wire is denoted by L and the coverage of the superconductor by c_0 .



(a) $V_{sc} = 0 \text{ V}$, $V_g = 0.3 \text{ V}$

(b) $V_{sc} = 0.2 \text{ V}$, $V_g = -0.2 \text{ V}$

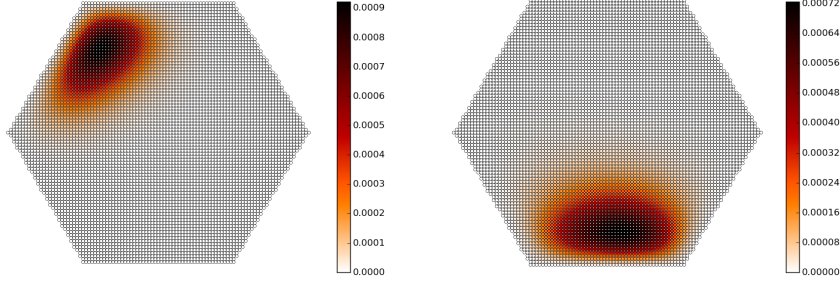
Figure 5.10: This image shows the energy potential for electrons in electron volt for the hexagonal nanowire. The influence of the superconductor can be seen on the top left resulting of an energy of 0 and -0.2 respectively. The gate introduces a voltage in the lower part of the nanowire. The system under consideration has $L = 100 \text{ nm}$ and $c_0 = 0 \text{ nm}$.



(a) p-renormalization

(b) k^4 -renormalization

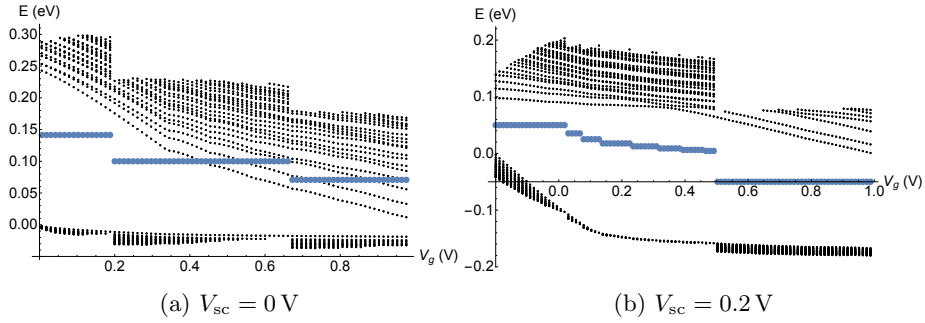
Figure 5.11: The figures above show the electron density in the nanowire for $V_g = 0.3 \text{ V}$ and $V_{sc} = 0 \text{ V}$. The spurious solutions were removed in different ways. The left plot corresponds to p-renormalization while the right plot corresponds to k^4 -renormalization with $\beta = 1 \text{ nm}^4 \text{ eV}$.



(a) $V_{sc} = 0.2 \text{ V}$, $V_g = -0.2 \text{ V}$

(b) $V_{sc} = 0.2 \text{ V}$, $V_g = 0.5 \text{ V}$

Figure 5.12: The wavefunction in a nanowire with $L = 100 \text{ nm}$ and $c_0 = 0 \text{ nm}$. The figures correspond to different values of the gate potential V_g . The Hamiltonian is diagonalized with $\beta = 1 \text{ eV nm}^4$.



(a) $V_{sc} = 0 \text{ V}$

(b) $V_{sc} = 0.2 \text{ V}$

Figure 5.13: Every point in this figure corresponds to an eigenstate in the nanowire. The x-axis denotes the gate voltage V_g . The voltage of the superconductor is $V_{sc} = 0 \text{ V}$ for **Fig. a** and $V_{sc} = 0.2 \text{ V}$ for **Fig. b**. The simulation automatically adjusted the parameter σ to find the eigenvalues around the gap which are shown as large blue dots (see Sec. 5.2). This causes block structure at the top of the figure.

conducting wavefunction now causes different behavior for positive and negative gate voltages which will be further discussed in Sec. 5.4.3.

The band structure depends on the voltages V_{sc} and V_g which in turn influences the spin-orbit interaction, but these voltages also change the gap of the system. It is interesting to study the development of the gap for different gate voltages, and the available states in the system are shown in Fig. 5.13 from which the gap can be inferred. For larger electric fields the gap closes, but the gate voltage for which the gap is maximal depends on the superconducting workfunction. The relevant regime for the simulations consists of those voltages where the gap has a finite value and hence Fig. 5.13 is used to determine this regime.

The resulting fields are stronger than the fields used in the previous section and have a significant effect on the wavefunction in the nanowire. Therefore the width of the nanowire is no longer a good measure for the effective width of the

quantum well states. From the explicit form of the wavefunction an effective width can be calculated by requiring that the variance of the position operator in the simulation and quantum well state must be equal:

$$\text{var}(\vec{r}_{\text{qw}}) = \text{var}(\vec{r}_{\text{sim}}). \quad (5.7)$$

The LHS of this equation is understood to describe a quantum well system with width L_{eff} and solving this equation yields an explicit value for this parameter.

The electric field needed to obtain a theoretical prediction is no longer unambiguously defined as the theory assumes a constant electric field (see Eq. (4.5)). The results in this section will therefore not be given in terms of r_{41}^{6c6c} but in terms of k_{so} which is unambiguously defined for the simulations. To obtain a theoretical prediction for k_{so} an effective field parameter is needed which is taken as

$$E_{\text{eff}} = \sqrt{\langle \psi | E_x | \psi \rangle^2 + \langle \psi | E_y | \psi \rangle^2}. \quad (5.8)$$

The parameters L_{eff} and E_{eff} can be obtained from the functional form of the wavefunction which follows from the Schrödinger-Poisson solver. Theoretical predictions can be made for the numerical simulations set forth in this section. First the case of $V_{\text{sc}} = 0 \text{ V}$ is investigated followed by an investigation of $V_{\text{sc}} = 0.2 \text{ V}$. Finally the influence of the parameter c_0 is studied where the numerical simulations are dropped for they would be too time consuming to simulate and only the theoretical prediction is calculated.

5.4.1 Results for $V_{\text{sc}} = 0 \text{ V}$

For this subsection the effective voltage of the superconductor is set to zero to obtain an initial result for the simulated electric fields. From Fig. 5.13a the range for the gate voltage is obtained and simulations are done for $0 \text{ V} < V_{\text{g}} \leq 0.8 \text{ V}$. The spin orbit interaction strength is obtained for the first six subbands in terms of k_{so} . The growth direction in this simulation is taken as [100]. The theoretical result is given for the bulk system given by Eq. (3.19) and for the subband theoretical prediction for $L = L_{\text{eff}}$ given by Eq. (3.39) for the first subband.

The result of the numerical simulation and the theoretical prediction agree well. The trend predicted by theory is followed by the numerical simulation and it would be possible to extrapolate the theoretical predictions to obtain a similar result for higher values of V_{g} . Higher subbands exhibit smaller spin orbit interaction, in agreement with Fig. 5.3b. The corresponding spin-orbit length at $V_{\text{g}} = 0.8 \text{ V}$ is approximately $l_{\text{so}} = 200 \text{ nm}$.

5.4.2 Results for $V_{\text{sc}} = 0.2 \text{ V}$

Once the fields have been calculated, it is possible to obtain the theoretical prediction, as shown in the previous subsection. Here, similar calculations are made where the superconducting wavefunction is taken into account by setting $V_{\text{sc}} = 0.2 \text{ V}$. Again a bulk prediction and a subband prediction are obtained from these calculations which can both be compared to the numerical simulations.

The numerical simulations were done for $0.2 \text{ V} \leq V_{\text{g}} \leq 1.0 \text{ V}$ for a nanowire system with $L = 100 \text{ nm}$ and $c_0 = 0 \text{ nm}$. The simulation is performed for both growth direction [100] and [111] but only the first subband is calculated. The result of this simulation is shown in Fig. 5.15.

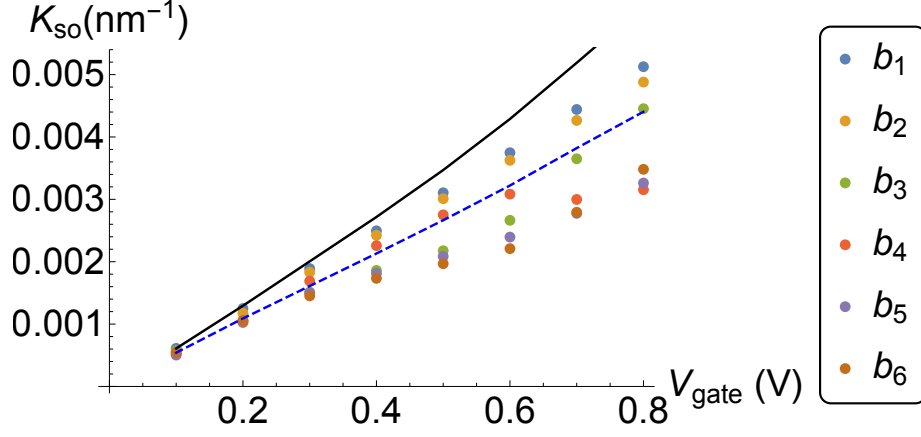


Figure 5.14: The spin-orbit momentum k_{so} for the first six subbands of a nanowire of $L = 100$ nm and $c_0 = 0$ nm. The field is simulated for $V_{sc} = 0$ V and various values for V_g . The solid black line denotes the bulk theoretical prediction of Eq. (3.19). The dashed blue line denotes the theoretical prediction of Eq. (3.39).

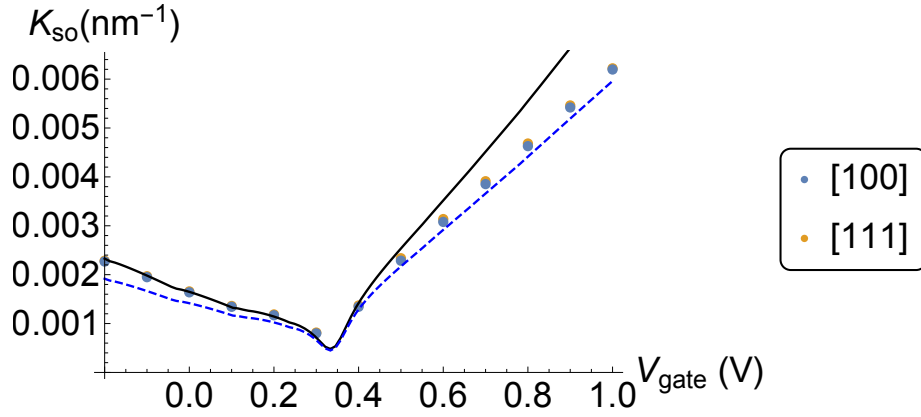


Figure 5.15: The spin-orbit momentum k_{so} for a nanowire of $L = 100$ nm and $c_0 = 0$ nm. The effective voltage of the superconductor is taken as $V_{sc} = 0.2$ V while the voltage of the backgate is varied over the \hat{x} -axis. The growth direction of the wire is [100] for the blue dots and [111] for the orange dots. Similar to Fig. 5.14 the solid black line denotes the bulk theoretical prediction of Eq. (3.19) and the dashed blue line denotes the theoretical prediction of Eq. (3.39).

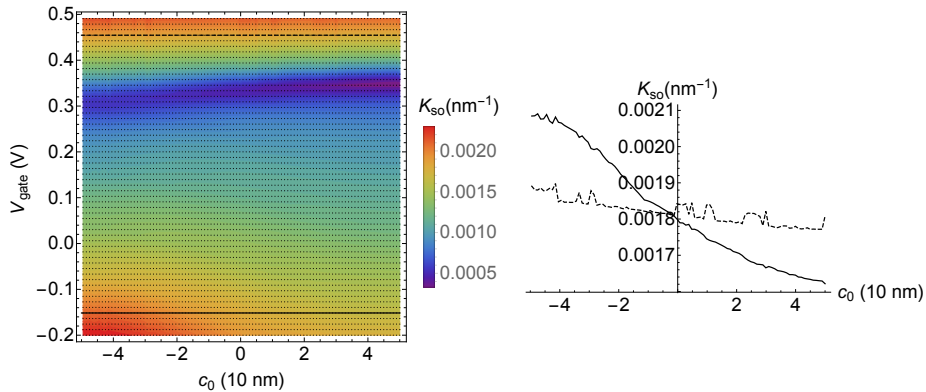


Figure 5.16: Left shows the value of k_{so} resulting from Eq. (3.39) for various gate voltages on the \hat{y} -axis and coverage parameters c_0 on the \hat{x} -axis. The parameter c_0 is denoted in tens of nanometers. Every black dot in the picture corresponds to a data point from which the contour plot is calculated. The right plot shows two line traces corresponding to the dashed and dotted line in the left picture.

The theoretical predictions matches the simulations again very well and the difference between the two growth direction is not significant for this simulation. This increases the confidence that growth direction parameter can be ignored in these simulations as previously announced in Sec. 5.3.3. In contrast to the simulation of the previous subsection more fields are calculated than are used for the numerical simulation, as the numerical simulation is the most time consuming part of these calculations. This reveals that the lowest point for the spin-orbit interaction strength is obtained for $V_g = 0.33$ V. This minimum arises when the average electric field over the wavefunction of the conduction band electrons is smallest. The results from the electric field simulations show that this happens at $V_g = 0.33$ V.

5.4.3 Effects of superconducting coverage

For this subsection, the numerical simulations are dropped as they would be too time consuming to generate the result for this subsection. From the previous two subsection it can be deduced that the results of the theoretical prediction and the numerical calculation are sufficiently close in order to get a good understanding of the spin-orbit interaction by only finding the theoretical prediction.

In this section the effect of the superconducting coverage parameter c_0 is studied. For many different values of V_g and c_0 the parameter k_{so} is calculated keeping $V_{\text{sc}} = 0.2$ V fixed. The formula for calculating the theoretical prediction is taken as the subband formula for r_{41}^{6c6c} form Eq. (3.39) corresponding to the blue dashed line in Fig. 5.13a and Fig. 5.15. A contour plot is shown together with two line traces in Fig. 5.16. The two line traces correspond to one negative and one positive gate voltages, chosen such that k_{so} is roughly equal in the two cases.

The figure shows similar behavior as Fig. 5.15 which exhibits a minimum at $V_g = 0.33$ V. For positive gate voltages the effect of changing the superconducting coverage is small shown by a dashed line. For negative gate voltages however,

the effect of changing c_0 is much larger. This can also be understood from the physical picture of Fig. 5.12 where for positive gate voltages the wavefunction is far away from the superconductor and the influence of the superconductor should hence be limited. For negative gate voltages the wavefunction is very close to the superconductor and a much larger effect from the parameter c_0 is expected.

6 Conclusion and Outlook

6.1 Conclusion

In this thesis the effect of symmetry in quantum mechanics is investigated. Representation theory is used to combine symmetry with quantum mechanics. This leads to the different representations for spin of particles and exchange statistics of bosons and fermions. By extending the permutation group it is found that anyons can have very different exchange statistics than ordinary bosons or fermions. Symmetry also imposes conditions on the Hamiltonian which is exemplified by the theory of invariants. This theory is then used to construct the 8×8 Kane Hamiltonian which is used to describe semiconductor systems. By studying the symmetry explicitly, it is found that not only Rashba spin-orbit interaction, but also Dresselhaus spin-orbit interaction can contribute to the spin splitting in [111] nanowires.

The Rashba spin orbit effect is studied by applying Löwdin partitioning to the Kane Hamiltonian and using the theory of invariants. Doing the partitioning explicitly for bulk systems and confined systems yields a theoretical prediction for the Rashba coefficient r_{41}^{6c6c} . The bulk formula agrees with reference [29], while the confined formula has a small difference. An important result is that the structure of the prediction for the 1-dimensional nanowire and 2-dimensional quantum well systems is the same. The actual prediction can differ because the energies of the eigenstates is different, which leads to the difference between 1-dimensional and 2-dimensional systems from the point of view of this theory.

The problem of spin-orbit interaction was then simulated in 2-dimensional quantum well systems. The resulting states in the system approximated particle in a box states for increasing L . The bare mass for the conduction band is negative in the Kane Hamiltonian. This leads to a closing of the gap of the semiconductor at a finite value for the wavevector in the numerical simulations. To prevent the resulting spurious solutions, two methods were studied. First, p-renormalization turned out not to work in the situation of nanowire systems, hence this method was dropped. Instead k^4 -renormalization is used to prevent the spurious solutions. With k^4 -renormalization the numerical result for the spin-orbit interaction strength is well approximated by theory.

Subsequently, the problem was transformed to the 1-dimensional nanowire case. For different parameters the Rashba coefficient is obtained such that a comparison with theory can be made. For constant electric fields various parameter dependencies are studied and all found reasonable agreement with theory. Most notably, the theoretical formula takes material, subband and system width into account which can be used to predict the behavior of the system for different combinations of these parameters.

For simulated electric fields, an effective width and effective field are calculated from the functional form of the electric field and the wavefunction. This results in good agreement between the numerical simulations and the theoretical prediction. This result holds for simulations with and without an effective voltage on the superconductor. These results suggest that the theoretical prediction is a good measure for the value obtained from numerical simulations. Hence, dependency on the superconducting coverage of the wire is studied by calculating the theoretical prediction for various values of c_0 .

6.2 Outlook

The nanowire simulations in this thesis are calculated on a 2-dimensional lattice. It is implicitly assumed that the third direction is an infinite, homogeneous direction and that the gates under the nanowire are also infinitely long. This implication does not represent reality and it is not obvious if this is a reasonable approximation. Therefore the 3-dimensional structure of the nanowire with gates must be studied. It is however not computationally achievable to calculate the 8×8 Kane Hamiltonian for a 3-dimensional nanowire. If it would be possible, however, to find the electric fields in 3-dimensional structures, the theoretical predictions of this thesis can be applied to those results to yield the Rashba spin-orbit interaction strength in these 3-dimensional structures. This would then enable the more accurate prediction of spin orbit interaction in nanowire systems.

Secondly, the results of this thesis should be compared to experiment. By comparing to experiments, the theory, simulations and the experiment can be understood better. In this thesis, the theory matches the simulations reasonably well and experiments could verify these results independently.

Finally, the Dresselhaus spin-orbit interaction in [111]-nanowires predicted in Sec. 3.6 must be studied. A similar theoretical prediction should be obtained and verified by numerics by implementing the 14×14 Kane Hamiltonian.

Acknowledgements

First, I would like to thank my supervisors. Rembert Duine, thank you for enabling me to perform my Master research in Delft. Your help and enthusiasm have been a big support while working on this thesis. Next, I would like to thank Michael Wimmer for the daily supervision in Delft. I have greatly appreciated all the insight and discussions in the past year. I was very impressed by the nature of the supervision that left me energized and motivated after every meeting. The speed at which you were able to spot mistakes, yet also point out positive features during these meetings was incredible. Leo Kouwenhoven, thank you for allowing me to perform research in the QuTech Topo team. I have felt that being surrounded by all the people in the lab, I was able to learn a lot about both theoretical and experimental physics. I would like to especially thank you for enabling me to go to Les Houches, an experience that I will never forget. I have greatly appreciated the supervision by Maja Cassidy. Your method of supervision allowed me to get the most out of myself. You always called a spade a spade such that it was always clear what I could improve. You showed me that by not being satisfied prematurely, the work can improve a lot. I would also like to thank you explicitly for introducing me to the field of experimental physics, showing and explaining to me many of the steps involved in the experiments.

I would like to thank Anton Akhmerov for the insight in *Kwant* and physics in general. I have appreciated your concise but tremendously correct answers to many of my questions. I wish to acknowledge the extensive help offered by Rafał Skolasiński and Adriaan Vuik, without you, my research would not have been possible. Adriaan, thank you for allowing me to use your program to calculate the electric fields and your help implementing it. Rafał, thank you for getting me started with *Kwant* and Python in general and allowing me to use your code

for the $H_{8 \times 8}$ Kane Hamiltonian, but my thanks would not be complete without thanking you for debugging the HPC at any hour of the day or, worst of all, debugging dolfin after nearly every update of the HPC.

James Kroll, I have especially enjoyed our collaboration of the past year and I must thank you for training me in the cleanroom. Also, your insight on the language used in my thesis has helped to improve it a lot. I look forward to working with you in the coming month, let's get that T1! Willemijn Uilhoorn, I wanted to thank you for all discussions we have had. The fact that you are never satisfied with a vague answer has increased my fundamental understanding of many papers and experiments. I liked collaborating on the Alazar driver, I think we made a beautiful piece of software. I have also greatly enjoyed our discussions and strolls during the summer school in Les Houches. Stijn Balk, thank you for the many fun and enlightening talks we had, I wish you a lot of luck with completing your own thesis. Francesco Borsoi, your motivation and spirit work contagiously, lifting my mood every time I see you looking at some nice results. Thanks to all my fellow master students. I am very sorry for not joining you for lunch nearly as often as I should have, but I do thank you all for your support and varied conversations when I did leave QC-lab.

Finally, I would like to thank my parents, Annelies Steehouder and Frank de Jong. Upon visiting you I could always count on a good meal and food for thought which would enable me to resume working with renewed energy and inspiration.

A Symbols and Notation

This appendix is a summary of all notation used in this thesis together with the values of the constants relevant for this research. The notation of point groups and their representations is not included, but can be found in Reference [33]. The parameters for the 8×8 Kane Hamiltonian such as P , γ_i , etc can be found in Reference [29]. The notation $\vec{\tau}$ means the three dimensional vector, such that $\vec{\sigma}$ only means $(\sigma_x, \sigma_y, \sigma_z)$.

Symbol	Name
$\mathbb{1}$	The identity operator
a	Lattice constant
\vec{B}	Magnetic field
\mathcal{B}_n	The braid group on n strands
β	Parameter controlling the k^4 -renormalization
c	Speed of light
c^\dagger, c	Fermion creation/annihilation operator
\mathcal{C}	Charge conjugation
c_0	Parameter for the superconducting coverage of the nanowire
Δ	Superconducting gap
$\Delta_{ij}^{b_1 b_2}$	Energy difference between band b_1 subband i and band b_2 subband j
D_s^\pm	Representation of \mathcal{R}
E	Energy or energy difference
\vec{E}	Electric field
E_{so}	Parameter of the spin-orbit interaction, see Fig. 1.3a
γ	Majorana zero mode operator
$\text{GL}(V)$	General linear group on a vector space V
\mathcal{H} or H	Hamiltonian
\hbar	Reduced Planck constant
i	Imaginary unit $\sqrt{-1}$
k_{so}	Parameter of the spin-orbit interaction, see Fig. 1.3a
L	Width of quantum well and nanowire systems
m_b	Effective mass of band b
\mathcal{P}	Parity transformation
\mathcal{P}_n	Pure braid group on n elements
σ	Parameter for the numerical diagonalization algorithm
σ_i	Exchange operator of elements i and $i + 1$ in the context of S_n or \mathcal{B}_n
σ_i	Pauli matrices, where $\sigma_0 = \mathbb{1}$
r_{41}^{6c6c}	Rashba spin-orbit coefficient
S_n	Permutation group on n elements
$\text{SO}(3)$	Special orthogonal group in three dimensions
$\text{SU}(2)$	Special unitary group in two dimensions
\mathcal{T}	Time reversal
\mathbb{Z}_2	The unique group of order two represented as addition modulo 2

B Units

The relevant quantities in this thesis are all on the level of quantum mechanical phenomena. With normal *SI* units, the results of this thesis would be expressed by extremely small (or large) numerical prefactors. To circumvent this, a new system of units is introduced together with a conversion table.

There are four relevant physical base dimensional which are length, mass, time and current. These dimensions are denoted by respectively L, M, T and I [38]. A corresponding unit is chosen for each of these dimensions.

For the length dimension L the quantities are expressed in units of 1 nm and for the mass dimension M the values are expressed in units of electron mass, m_e .

Next, the time and current units are defined such that the electrical charge of an electron is 1 and the unit of energy becomes eV. Imagine a stationary electron that is subsequently accelerated by an electric field of 1 V, the time t_e it takes for the electron to travel a distance of $\sqrt{2}$ nm is taken as the unit for the time dimension T. The unit for the current dimension I is then straightforwardly defined as one electron charge e per unit of time t_e . This leads to the following conversion table

Dimension	new unit	conversion to <i>SI</i> unit
L	nm	1×10^{-9} m
M	m_e	$9.109\,382\,91 \times 10^{-31}$ kg
T	t_e	$2.384\,46 \times 10^{-15}$ s
I	A_e	$6.719\,25 \times 10^{-5}$ A

With the units defined, the important constants of nature can be defined in terms of these units. The electrical charge in the new units is

$$1A_e \cdot 1t_e = 1e \quad (\text{B.1})$$

This means that the electrical charge is denoted in units of e . Similar for energy it holds that

$$1 \frac{m_e \text{nm}^2}{t_e^2} = 1 \text{eV} \quad (\text{B.2})$$

such that energy is expressed in eV in this system of units. Finally the value for \hbar must be calculated by

$$\hbar = 1.054\,571\,73 \times 10^{-34} \text{ J s} = 0.276\,043 \text{ eV}t_e. \quad (\text{B.3})$$

C Exchange statistics of Majorana zero modes

In this section it will be shown that the Majorana zero modes obey non-abelian braiding statistics starting from the following assumptions

$$\gamma_i = \gamma_i^\dagger \quad (\text{C.1})$$

$$\{\gamma_i, \gamma_j\} = 2\delta_{ij} \quad (\text{C.2})$$

$$\text{parity conservation.} \quad (\text{C.3})$$

Consider a state with two Majorana zero modes. By varying the Hamiltonian adiabatically, the two Majorana fermions can be exchanged. The time-dependent Hamiltonian at time t is denoted by $H(t)$ and time-dependent Majorana operators are introduced as

$$\gamma_i(t) = U^\dagger(t)\gamma_i U(t), \quad (\text{C.4})$$

where the time-evolution operator is

$$U(t) = e^{-\frac{i}{\hbar} \int_{t_0}^t H(t') dt'}. \quad (\text{C.5})$$

If the square of Eq. (C.4) is taken, this results in

$$\gamma_i(t)^2 = U^\dagger(t)\gamma_i U(t)U^\dagger(t)\gamma_i U(t) = U^\dagger(t)\gamma_i\gamma_i U(t) = U^\dagger(t)U(t) = 1. \quad (\text{C.6})$$

The time dependence considered here corresponds to a exchange operation, hence the final Hamiltonian must be equal to the initial Hamiltonian. That the exchange is adiabatic means that all states transform to the corresponding states of the final Hamiltonian. In other words, the final Majorana operators are given by

$$\gamma_2(t_1) = s_1\gamma_1(t_0) \quad (\text{C.7})$$

$$\gamma_1(t_1) = s_2\gamma_2(t_0). \quad (\text{C.8})$$

Combined with Eq. (C.6) and Eq. (C.2) this leads to

$$1 = (s_i\gamma_i)^2 = s_i^2 \quad (\text{C.9})$$

To show that the exchange operation is non-abelian, it remains to be shown that $s_1s_2 = -1$. Fermion creation operators can be constructed from the two Majorana operators by

$$c^\dagger = \gamma_1 + \imath\gamma_2. \quad (\text{C.10})$$

If U is the operator exchanging the two Majorana zero modes, this means that

$$U^\dagger d^\dagger U = s_2\gamma_2 + \imath s_1\gamma_1. \quad (\text{C.11})$$

Assume, leading to contradiction, that s_1 equals s_2 which would result in

$$U^\dagger d^\dagger U = -\imath s_1 d, \quad (\text{C.12})$$

or equivalently

$$d^\dagger U = -\imath s_1 U d. \quad (\text{C.13})$$

Majorana zero modes have no energy and commute with the Hamiltonian. This means that $d^\dagger d$ also commutes with the Hamiltonian and hence the ground state can be taken to be a simultaneous eigenstate of H and $d^\dagger d$ which is denoted with $|0\rangle$ where $d|0\rangle = 0$. With this notation, it holds that

$$d^\dagger U |0\rangle = -\imath s_1 U d |0\rangle = 0. \quad (\text{C.14})$$

If $|0\rangle$ has a definite parity, then $U|0\rangle \propto |1\rangle$ has the opposite parity and this contradicts the conservation of parity. Hence our assumption that $s_1 = s_2$ must be false and this leads to $s_1s_2 = -1$.

Hence exchanging two Majorana zero modes is non-abelian. Repeating the exchange twice does not give the identity as for normal bosons and fermions, but it gives minus the identity instead.

D Derivation r_{41}^{6c6c}

the goal of Löwdin partitioning is to make a basis transformation such that the Hamiltonian becomes block diagonal. A detailed explanation of Löwdin partitioning is beyond the scope of this thesis. A good explanation of this method can be found in reference [29]. In this appendix the process to obtain Eq. (3.39) from the 8×8 Kane Hamiltonian will be explained. The first step in subband Löwdin perturbation is to divide the Hamiltonian in two sets of states, A and B . Set A consists of all conduction band states from H_{6c6c} and set B consists of all valence band states from H_{8v8v} and H_{7v7v} . To get an effective Hamiltonian for the conduction band the Hamiltonian can be expanded as

$$H_{2 \times 2} = H^{(0)} + H^{(1)} + H^{(2)} + H^{(3)} + \dots, \quad (\text{D.1})$$

where $H^{(n)}$ depends on the full 8×8 Kane Hamiltonian. In order to define $H^{(n)}$, the original Hamiltonian must be split into a diagonal Hamiltonian, and a part containing all other terms which is treated as a small perturbation of the diagonal Hamiltonian. The diagonal Hamiltonian is taken as

$$H_0 = \begin{pmatrix} H_{6c6c}^d & 0 & 0 \\ 0 & H_{8v8v}^d & 0 \\ 0 & 0 & H_{7v7v}^d \end{pmatrix}, \quad (\text{D.2})$$

where $H_{bb}^d = -\frac{\hbar^2}{2m_b} \nabla^2 + V(\vec{r})$. The other part is taken as

$$H' = H_{8 \times 8} + e\mathbb{1}\vec{E} - H_0. \quad (\text{D.3})$$

The matrices here should be interpreted as matrices of infinite dimensional matrices as explained in Sec. 3.5 and Eq. (3.30).

The Rashba coefficient is contained in the third order of the expansion of $H_{2 \times 2}$. Explicitly define

$$(t_1)_{mi,m'i'} = \sum_{m''i'',lj} \left(\frac{H'_{mi,lj} H'_{lj,m''i''} H'_{m''i'',m'i'}}{\Delta_{m'i',lj} \Delta_{m''i'',lj}} + \frac{H'_{mi,m''i''} H'_{m''i'',lj} H'_{lj,m'i'}}{\Delta_{mi,lj} \Delta_{m''i'',lj}} \right) \quad (\text{D.4})$$

and

$$(t_2)_{mi,m'i'} = \sum_{lj,l'j'} \left(\frac{H'_{mi,lj} H'_{lj,l'j'} H'_{l'j',m'i'}}{\Delta_{mi,lj} \Delta_{mi,l'j'}} + \frac{H'_{mi,lj} H'_{lj,l'j'} H'_{l'j',m'i'}}{\Delta_{m'i',lj} \Delta_{m'i',l'j'}} \right) \quad (\text{D.5})$$

such that $H^{(3)}$ can be written as

$$H_{mi,m'i'}^{(3)} = -\frac{1}{2}(t_1)_{mi,m'i'} + \frac{1}{2}(t_2)_{mi,m'i'}. \quad (\text{D.6})$$

In these equations m , m' and m'' denote the conduction band and i , i' and i'' the corresponding subband numbers. The variables l and l' denote one of the valence bands (light hole, heavy hole or spin splitoff) and j and j' the corresponding subband numbers. These indices make explicit the fact that H' is an infinite dimensional matrix and hence does not commute. Keeping track of the indices is most easily done by a computer program such as *Mathematica*, *Maple*, etc.

In the rest of this section, the steps to arrive at Eq. (3.39) is described without giving intermediate results as that would lead to many pages of derivation.

The first step is to realize that the only conduction band of interest is the 6c band and the subband indices i and i' must be equal. Every operator in Eq. (D.6) allows distributivity hence the distributivity law is applied to the plus operators occurring in Eq. (D.3). This leads to an expression of 33 terms.

Next, all terms that are not proportional to the electric charge e are dropped as these terms can never contribute to the Rashba coefficient, doing so result in a expression of only 9 of the original 33 terms. To continue, the definition of the 8×8 Kane Hamiltonian must be used. All parts of this Hamiltonian are defined in terms of σ Pauli matrices. Once this is done, distributivity is again applied over every plus operation and all conjugate transpose operations in the equation are explicitly be performed.

The products of sigma matrices can also be calculated and every term that is not proportional to either σ_x , σ_y or σ_z is removed as these terms cannot contribute to r_{41}^{6c6c} . Doing so results in an expression consisting of 42 terms.

Now, the explicit form of the spin-orbit term is used and σ_y and σ_z are set to zero while \vec{E} is set to $E_z \hat{z}$. For each term that is left in the equation at this point, the three H' matrices change into \hat{z} , \hat{k}_z and $\mathbb{1}$ in some permutation, but each one occurring exactly once. These operators still act on the basis states used to define Eq. (3.30). Some terms, however, only contain the identity operator such that the two basis states act on one another and this results by assumption in a delta-function. Hence each term left in the equation is proportional to $\langle \psi_{ci}|z|\psi_{bj} \rangle \langle \psi_{bj}|k_z|\psi_{ci} \rangle$ or $\langle \psi_{ci}|k_z|\psi_{bj} \rangle \langle \psi_{bj}|z|\psi_{ci} \rangle$ for some band b . After enumerating every term, Eq. (3.39) is obtained.

References

- [1] Ettore Majorana. Teoria simmetrica dell'elettrone e del positrone. *Il Nuovo Cimento*, 14:171–184, 1937.
- [2] Frank Wilczek. Majorana returns. *Nature Physics*, 5(9):614–618, sep 2009.
- [3] A Yu Kitaev. Unpaired majorana fermions in quantum wires. *Physics-Uspekhi*, 44(10S):131, 2001.
- [4] Frank Wilczek. Quantum mechanics of fractional-spin particles. *Physical Review Letters*, 49(14):957–959, 1982.
- [5] P.W. Shor. Algorithms for quantum computation: discrete logarithms and factoring. *Proceedings 35th Annual Symposium on Foundations of Computer Science*, pages 124–134, 1994.
- [6] L K Grover. A fast quantum mechanical algorithm for database search. In *Proceedings, 28th Annual ACM Symposium on the Theory of Computing (STOC)*, pages 212–219. ACM, 1996.
- [7] Richard P Feynman. Simulating physics with computers. *International Journal of Theoretical Physics*, 21(6-7):467–488, 1982.
- [8] Meng Cheng, Roman M. Lutchyn, and S. Das Sarma. Topological protection of Majorana qubits. *Phys. Rev. B*, 85(16):165124, 2012.
- [9] V. Mourik, K. Zuo, S. M. Frolov, S. R. Plissard, E. P. a. M. Bakkers, and L. P. Kouwenhoven. Signatures of Majorana Fermions in Hybrid Superconductor-Semiconductor Nanowire Devices. *Science*, 336(6084):1003–1007, 2012.
- [10] Martin Leijnse and Karsten Flensberg. Introduction to topological superconductivity and majorana fermions. *Semiconductor Science and Technology*, 27(12):124003, 2012.
- [11] D. a. Ivanov. Non-Abelian statistics of half-quantum vortices in p-wave superconductors. *Physical Review Letters*, 86:268–271, 2001.
- [12] David J. Clarke, Jay D. Sau, and Sumanta Tewari. Majorana fermion exchange in quasi-one-dimensional networks. *Phys. Rev. B*, 84:035120, Jul 2011.
- [13] B. Coecke. *New Structures for Physics*. Springer-Verlag, 2011.
- [14] Alexei Kitaev. Anyons in an exactly solved model and beyond. *Annals of Physics*, 321(1):2–111, 2006.
- [15] Chetan Nayak, Steven H. Simon, Ady Stern, Michael Freedman, and Sankar Das Sarma. Non-Abelian anyons and topological quantum computation. *Reviews of Modern Physics*, 80(September):1083–1159, 2008.
- [16] S B Bravyi. Universal quantum computation with the $\nu=5/2$ fractional quantum Hall state. *Physical Review A*, 73(4):42313, 2006.

- [17] Jason Alicea, Yuval Oreg, Gil Refael, Felix von Oppen, and Matthew P. a. Fisher. Non-Abelian statistics and topological quantum information processing in 1D wire networks. *Nature Physics*, 7(5):412–417, 2011.
- [18] F. Hassler, a. R. Akhmerov, and C. W J Beenakker. The top-transmon: A hybrid superconducting qubit for parity-protected quantum computation. *New Journal of Physics*, 13(9):095004, 2011.
- [19] B van Heck, A R Akhmerov, F Hassler, M Burrello, and C W J Beenakker. Coulomb-assisted braiding of Majorana fermions in a Josephson junction array. *New Journal of Physics*, 14(3):035019, 2012.
- [20] T. Hyart, B. Van Heck, I. C. Fulga, M. Burrello, a. R. Akhmerov, and C. W J Beenakker. Flux-controlled quantum computation with Majorana fermions. *Physical Review B - Condensed Matter and Materials Physics*, 88(3):1–20, mar 2013.
- [21] G. L. Bir and G. E. Pikus. *Symmetry and Strain-induced Effects in Semiconductors*. Keter Publishing House Jerusalem Ltd., 1974.
- [22] Adriaan Vuik. Effects of the electrostatic environment on the properties of Majorana devices. Master’s thesis, Delft University of Technology, the Netherlands, 2014.
- [23] Simon L. Altmann. *Rotations, Quaternions and Double Groups*. Dover Publications, Inc., 2005.
- [24] M. S. Dresselhaus, G Dresselhaus, and A Jorio. *Group Theory Application to the Physics of condensed Matter*. Springer-Verlag, 2008.
- [25] Roe Goodman and Nolan R. Wallach. *Symmetry, Representations, and Invariants*. Springer-Verlag, 2009.
- [26] E.P. van den Ban. Lie groups. <http://www.staff.science.uu.nl/ban00101/lecnot.html>, 2010.
- [27] Frank Wilczek. *Fractional Statistics and Anyon Super Conductivity*. World Scientific, 1990.
- [28] Morton Hamermesh. *Group Theory and Its Application to Physical Problems*. Publishing Company Inc, 1962.
- [29] R. Winkler. *Spin-Orbit Coupling Effects in Two-Dimensional Electron and Hole Systems*. Springer-Verlag, 2003.
- [30] D.J.Griffiths. *Introduction to Quantum Mechanics*. Pearson Education, second edition, 2005.
- [31] Roger R. Haar and L. J. Curtis. The Thomas precession gives $ge-1$, not $ge/2$. *American Journal of Physics*, 55(1987):1044, 1987.
- [32] M.E. Peskin and D.V. Schroeder. *An Introduction To Quantum Field Theory*. Westview Press, 1995.
- [33] G. F. Koster, J. O. Dimmock, R. G. Wheeler, and H. Statz. *Properties of the Thirty-Two Point Groups*. M.I.T. Press, 1963.

- [34] Jun-Wei Luo, Lijun Zhang, and Alex Zunger. Absence of intrinsic spin splitting in one-dimensional quantum wires of tetrahedral semiconductors. *Phys. Rev. B*, 84:121303, Sep 2011.
- [35] I. van Weperen, B. Tarasinski, D. Eeltink, V. S. Pribiag, S. R. Plissard, E. P. A. M. Bakkers, L. P. Kouwenhoven, and M. Wimmer. Spin-orbit interaction in InSb nanowires. *Physical Review B*, 91(20):201413, 2015.
- [36] Christoph W Groth, Michael Wimmer, Anton R Akhmerov, and Xavier Waintal. Kwant: a software package for quantum transport. *New Journal of Physics*, 16(6):063065, 2014.
- [37] William H. Press, Saul A. Teukolsky, William T. Vetterling, and Brian P. Flannery. *The book Numerical Recipes: The Art of Scientific Computing*. Cambridge University Press, third edition, 2007.
- [38] Bureau international des poids et mesures. *Le Système international d'unités*. 8 edition, 2006.